7-2020

Reynolds-stress modeling of cluster-induced turbulence in particle-laden vertical channel flow

Michael C. Baker
Iowa State University

Rodney O. Fox
Iowa State University, rofox@iastate.edu

Bo Kong
Ames Laboratory

See next page for additional authors

Reynolds-stress modeling of cluster-induced turbulence in particle-laden vertical channel flow

Abstract

Particle-laden flow in a vertical channel was simulated using a Reynolds-averaged Navier-Stokes two-fluid model including a Reynolds-stress model (RSM). Two sets of cases varying the overall mass loading were done using particle sizes corresponding to either a large or small Stokes number. Primary and turbulent statistics extracted from counterpart Eulerian-Lagrangian and Eulerian-Eulerian anisotropic-Gaussian simulations were used to inform parameters and closures applied in the RSM. While the behavior at the center of the channel compared well with the other simulations, including the transition from fully developed turbulent flow to relaminarization to cluster-induced turbulence as the mass loading increased, the behavior close to the wall deviated significantly. The primary contributor to this difference was the application of a uniform drag coefficient, which resulted in the RSM overpredicting the fluid-phase turbulent kinetic energy close to the wall. When considering small Stokes particles, the RSM at greater mass loadings reproduced the transient clustering observed in the other models. This was not observed using larger particles.

Disciplines

Complex Fluids | Fluid Dynamics

Comments

This article is published as Baker, M. C., R. O. Fox, B. Kong, J. Capecelatro, and O. Desjardins. "Reynolds-stress modeling of cluster-induced turbulence in particle-laden vertical channel flow." *Physical Review Fluids* 5, no. 7 (2020): 074304. DOI: 10.1103/PhysRevFluids.5.074304. Posted with permission.

Authors

Michael C. Baker, Rodney O. Fox, Bo Kong, Jesse Capecelatro, and Olivier Desjardins

Reynolds-stress modeling of cluster-induced turbulence in particle-laden vertical channel flow

M. C. Baker[*,†] and R. O. Fox
Department of Chemical and Biological Engineering, 618 Bissell Road, Iowa State University, Ames, Iowa 50011-1098, USA

B. Kong[†]
Ames Laboratory–U.S. Department of Energy, Ames, Iowa 50011-1015, USA

J. Capecelatro
Department of Mechanical Engineering, University of Michigan, Ann Arbor, Michigan 48109-2125, USA

O. Desjardins
Sibley School of Mechanical and Aerospace Engineering, Cornell University, Ithaca, New York 14853, USA

(Received 16 January 2020; accepted 16 June 2020; published 30 July 2020)

Particle-laden flow in a vertical channel was simulated using a Reynolds-averaged Navier-Stokes two-fluid model including a Reynolds-stress model (RSM). Two sets of cases varying the overall mass loading were done using particle sizes corresponding to either a large or small Stokes number. Primary and turbulent statistics extracted from counterpart Eulerian-Lagrangian and Eulerian-Eulerian anisotropic-Gaussian simulations were used to inform parameters and closures applied in the RSM. While the behavior at the center of the channel compared well with the other simulations, including the transition from fully developed turbulent flow to relaminarization to cluster-induced turbulence as the mass loading increased, the behavior close to the wall deviated significantly. The primary contributor to this difference was the application of a uniform drag coefficient, which resulted in the RSM overpredicting the fluid-phase turbulent kinetic energy close to the wall. When considering small Stokes particles, the RSM at greater mass loadings reproduced the transient clustering observed in the other models. This was not observed using larger particles.

DOI: 10.1103/PhysRevFluids.5.074304

I. INTRODUCTION

Particle-laden flows can be found in countless natural and man-made systems. Successful modeling helps in building an understanding of the underlying physical mechanisms behind the behavior observed. In an industrial context, a model is a useful tool in process design, optimization, troubleshooting, and scale-up applications. In this work, focusing on particle-laden vertical channel flow not only offers a direct analog to industrial processes such as circulating fluidized beds, it also provides an opportunity to obtain general insight on capturing the interaction of particle-laden flow and wall boundaries. There are a wide variety of approaches to modeling particle-laden

[*]mcbaker@iastate.edu
[†]Also at Center for Multiphase Flow Research and Education, 537 Bissell Road, Iowa State University, Ames, IA 50011-1096, USA.

systems, including direct numerical simulation (DNS), Eulerian-Lagrangian (EL) simulation, and two-fluid Eulerian-Eulerian simulation (EE). The challenge in choosing, building, and applying these modeling techniques is not only to be able to successfully resolve the particle-fluid phenomena present, but also to accomplish it at a scale relevant to the real-world application with reasonable computational times [1,2].

The DNS modeling technique involves directly solving the Newtonian equations of motion for each particle while ensuring that the Navier-Stokes and continuity equations are satisfied at every point in the fluid phase. Modeling considerations involved with DNS of particle-laden flow include the collisional and frictional interactions between particles as well as the boundary condition of the particle surface with the surrounding fluid [3]. Due to the intense computational cost of resolving the flow phenomena around each individual particle, DNS modeling of particle-laden flow is limited to simulating systems containing only a relatively small number of particles [4,5]. Despite this limitation, it is still invaluable in informing other modeling approaches when developing closures and validating their results.

To avoid the computational burden of fully resolving the flow fields around each particle in DNS, particles are often treated as point particles in simulations when the particle size is smaller than the Kolmogorov scale [6]. Lagrangian tracking of these point particles has been employed in a variety of particle-laden channel flow simulations. The effect of density ratio, mass loading, and particle inertia in turbulent channel flow was studied in [7]. Reference [8] studied the effect of particle Stokes number on near-wall turbulence using small, heavy particles. A closer examination of turbulent near-wall structures was the focus of [9]. In [10], particle drag and the effect of the channel wall were studied in dilute channel flow cases containing 500 and 4500 particles. Comparisons between experiments and simulations have been reported in [11] for relatively dilute turbulent channel flows, showing good agreement except near the walls.

EL simulations offer a further computational savings versus DNS techniques in modeling the particle phase as point particles immersed in fluid-phase Eulerian cells. Similar to DNS modeling, how the point particles collide and interact with each other and how the particles affect and are affected by the flow of the surrounding fluid must be addressed as modeling considerations [3,12]. In addition, how the particle volume in the fluid is treated must be defined, especially in cases where the volume of a particle ends up being a significant fraction of the volume of a fluid-phase cell [13]. Modeling the fluid phase in Eulerian cells offers the opportunity for further computational cost reductions through modeling fluid-phase turbulence using large eddy simulation (LES) or Reynolds-averaged Navier-Stokes (RANS) techniques [3]. An example of the former being applied to vertical turbulent particle-laden channel flow can be found in [14], which found the fluid-phase turbulence becoming more anisotropic with the addition of particles and demonstrated the significant impact of particle-particle interactions in suitably dense systems.

As initially developed by Anderson and Jackson [15], EE continuum models of particle-laden flow assume that the various properties of both the solid and fluid phases can be expressed as interpenetrating continua that interact with each other through the application of interphase drag terms [16]. Unlike point-particle DNS and EL techniques, the computational cost modeling the particle phase in Eulerian cells scales by the refinement of the domain rather than the number of particles, making it a more efficient choice when simulating systems containing a large number density of particles, such as fluidized beds. These drag terms must be closed through modeling, often by comparison with experimental data or more highly resolved simulation methods [17]. Another important consideration is the application of particle-particle interactions, often modeled through the kinetic theory of granular flow [18]. Finally, an array of multiphase turbulence models can also be applied to both Eulerian phases, including k–ε, k–ω, and the Reynolds-stress model (RSM) [19–22]. Application of any one of these turbulence models offers the tradeoff of exchanging the requirement for a high degree of refinement to resolve the turbulent instabilities in each phase with the need to accurately model its impact.

The presence of particles has shown to significantly alter the behavior of turbulence in the fluid phase. In extracting the Reynolds-stress energy budgets in vertical channel flow with and without

particles, Dritselis [23] demonstrated that the presence of particles dampens the production of fluid-phase turbulence. Furthermore, Ref. [24] showed the fluid-phase turbulence in a vertical channel transitioning from fully developed turbulence to a relaminarized state with fully dampened fluid-phase turbulence to a state of cluster-induced turbulence (CIT) as the particle-phase mass loading of the channel increased from a dilute particle concentration. CIT exists where the turbulence of the fluid phase is dominated by the presence of particle-phase clusters. Clustering is initially prompted by perturbations of the phase velocities inducing preferential concentrations in the particle phase [25]. Within these preferential concentrations, any applied uniform force such as gravity that has a disparate impact between the phases becomes more pronounced and self-reinforcing. Clusters develop as areas with more particles travel at a different velocity than more dilute regions, resulting in the more concentrated regions receiving a net increase of particles over time [26]. As in turbulent bubbly flows [21,27], these clusters have a strong influence on the turbulent statistics, leading to highly anisotropic Reynolds stresses and nonclassical near-wall turbulence profiles.

One aspect present in many existing applications of modeling particle-phase turbulence is that it conflates the spatially correlated turbulence of the particle phase arising from turbulent-stress production with the nonspatially correlated fluctuations from kinetic theory [20]. A modeling study was done in [28] using Lagrangian particle tracking that extracted and separated these two components and observed that the contribution of the fluctuating energy increases with increasing particle inertia. This led to the development of a system of Eulerian equations for the particle phase which solve for the turbulent kinetic energy and the fluctuating kinetic energy separately. Fox [20] took this further and developed the exact Reynolds-averaged equations for two-phase particle flow which separately solve for the turbulent kinetic energy of the particle phase and the fluctuating energy. An important addition made in [20] was factoring in collisions, expanding the possible reach of the model into moderately dense systems such as the recirculating components of a circulating fluidized bed. The particle turbulence was applied in the k–ε framework, while the fluctuating energy was solved through a granular energy balance from the kinetic theory of granular flow.

The RANS model in [20] was extended to account for the anisotropy of the Reynolds stresses in [19] and used to model cluster-induced turbulence in vertical channel flow [29]. Data obtained from a corresponding EL model was able to close the fluid-particle coupling terms vital in capturing the impact of CIT [13]. The RSM in [19] included modeling the uncorrelated fluctuating particle kinetic energy with an anisotropic granular pressure model that is able to track the granular particle energy as a tensor. Tracking the particle in this way provides the ability to capture the kind of anisotropy that characterizes many aspects of channel flow for the particle phase [30]. A second-order closure with very similar structure to the RSM in [19] has been developed for bubbly flow in [21].

While the model in our prior work [19] focused on modeling only the one-dimensional wall-normal profile of the vertical channel at steady state, this work expands on that through developing a transient RANS model including a RSM that also resolves the length of the vertical channel [19,29]. Unlike in single-phase RANS models for fully developed turbulent channel flows [31] (which yield time-independent solutions), fully developed channel flow with CIT leads to time-dependent volume-fraction fluctuations that dominant the flow physics. The application of steady-state equations to the full channel cannot capture this transient behavior, and its results would be indistinguishable from that seen in [19]. Additionally, turbulent statistics collected from both the previously applied EL model [13] and a highly refined EE anisotropic-Gaussian (EE-AG) model [30,32] of the channel are used as points of comparison and to inform the turbulent closures chosen for the model developed in this work.

II. REYNOLDS-STRESS MODEL FOR GAS-PARTICLE FLOWS

The model introduced in this work solves the Reynolds-averaged transport equations for the phase-averaged fluid and particle velocity, $\langle u_{i,f}\rangle_f$ and $\langle u_{i,p}\rangle_p$, phase-averaged fluid and particle Reynolds stresses, $\langle u'''_{f,i}u'''_{f,j}\rangle_f$ and $\langle u''_{p,i}u''_{p,j}\rangle_p$, fluid and particle turbulent dissipation, ε_f and ε_p, and phase-averaged particle pressure tensor, $\langle \mathcal{P}_{p,ij}\rangle_p$. The equations defined in this section are derived

from our previous work in [19,20,29]. The Reynolds-averaged particle-phase volume fraction, $\langle\alpha_p\rangle$, is developed using Eulerian continuum tracking based on the conservation of mass. The phase-averaging procedure for an arbitrary variable N and phase n is defined by $\langle N\rangle_n = \langle\alpha_n N\rangle/\langle\alpha_n\rangle$, where α_n is the n-phase volume fraction [29]. The Reynolds stresses are defined through splitting the velocity of each phase [20,33], $u_{f,i}$ and $u_{p,i}$, into a mean and a fluctuating component defined by $u_{f,i} = \langle u_{f,i}\rangle_f + u'''_{f,i}$ for the fluid phase and $u_{p,i} = \langle u_{p,i}\rangle_p + u''_{p,i}$ for the particle phase, where $u'''_{f,i}$ and $u''_{p,i}$ are the fluctuating velocities for the fluid and particle phases. For the interphase coupling, only the fluid drag on the particle is accounted for due to the relatively high density of the particles compared to the gas phase.

A. Mass

The closed equation for the particle-phase volume fraction (repeated Roman indices imply summation)

$$\frac{\partial\langle\alpha_p\rangle}{\partial t} + \frac{\partial\langle\alpha_p\rangle\langle u_{p,i}\rangle_p}{\partial x_i} = 0 \tag{1}$$

is developed through applying the mean and fluctuating component velocity splitting to the Eulerian conservation of particle mass and then ensemble-averaging the result [33]. The corresponding profile for the fluid volume fraction can be computed from the particle volume fraction profile: $\langle\alpha_f\rangle = 1 - \langle\alpha_p\rangle$. For CIT in a vertical channel, (1) generates nonuniform and nonstationary fields for $\langle\alpha_p\rangle$, which are only partially smoothed out as compared to α_p. These flow structures are reminiscent of shocks in gas dynamics and result from the relatively high particle-phase Mach number, $Ma_p = \frac{|\langle u_{p,i}\rangle_p|}{\Theta_p^{1/2}}$, where Θ_p is the granular temperature, defined as one-third of the trace of the particle pressure tensor, $\Theta_p = \frac{1}{3}\mathcal{P}_{kk}$.

B. Momentum

The Reynolds-averaged momentum transport equations for the fluid and particle phases, respectively, are

$$\frac{\partial\rho_f\langle\alpha_f\rangle\langle u_{i,f}\rangle_f}{\partial t} + \frac{\partial}{\partial x_j}\rho_f\langle\alpha_f\rangle(\langle u_{i,f}\rangle_f\langle u_{f,j}\rangle_f + \langle u'''_{f,j}u'''_{f,i}\rangle_f) = S_{f,\text{momentum},i} \tag{2}$$

and

$$\frac{\partial\rho_p\langle\alpha_p\rangle\langle u_{i,p}\rangle_p}{\partial t} + \frac{\partial}{\partial x_j}\rho_p\langle\alpha_p\rangle(\langle u_{i,p}\rangle_p\langle u_{p,j}\rangle_p + \langle u''_{p,j}u''_{p,i}\rangle_p) = S_{p,\text{momentum},i}, \tag{3}$$

where $S_{f,\text{momentum},i}$ and $S_{p,\text{momentum},i}$ are the summed totals of the source and sink terms for each phase [20,33]. These are defined as

$$S_{f,\text{momentum},i} = S_{f,\text{viscous},i} + S_{f,\text{pressure},i} + S_{f,\text{gravity},i} + S_{f,\text{drag},i} \tag{4}$$

for the fluid phase and

$$S_{p,\text{momentum},i} = S_{p,\text{viscous},i} + S_{p,\text{pressure},i} + S_{p,\text{collision},i} + S_{p,\text{gravity},i} + S_{p,\text{drag},i} \tag{5}$$

for the particle phase. Both phases include terms for the viscous stresses, phase pressure, gravitational hydrostatic force, and interphase drag. Only the particle phase includes an additional term for the collisional pressure.

The viscous stress source term applicable to both phases is defined as [20,30]

$$S_{n,\text{viscous},i} = \frac{\partial}{\partial x_j}\rho_n\langle\alpha_n\rangle\nu_n\left(\frac{\partial\langle u_{n,i}\rangle_n}{\partial x_j} + \frac{\partial\langle u_{n,j}\rangle_n}{\partial x_i} - \frac{2}{3}\frac{\partial\langle u_{n,k}\rangle_n}{\partial x_k}\delta_{ij}\right), \tag{6}$$

where ν_n is the viscosity for a given phase n. The viscosity for the particle phase is defined from the kinetic theory of granular flow as [1]

$$\nu_p = \frac{\sqrt{\pi}}{6(3-e_c)} d_p \sqrt{\Theta_p} \left(1 + \frac{2}{5}(1+e_c)(3e_c-1)\alpha_p g_0\right) + \frac{4(1+e_c)}{5\sqrt{\pi}} \alpha_p g_0 d_p \sqrt{\Theta_p}, \tag{7}$$

where Θ_p is the granular temperature, d_p is the particle diameter, g_0 is the radial distribution function, and e_c is the particle-particle collision restitution coefficient [30]. The radial distribution function is defined as

$$g_0 = \frac{1}{1 - \left(\frac{\alpha_p}{\alpha_{p,\max}}\right)^{1/3}}, \tag{8}$$

where $\alpha_{p,\max}$ is the solid fraction at maximum packing, defined in this study as equal to the perfectly uniform spheres packing limit [18]. In the turbulence model, (7) and (8) are evaluated using $\langle \alpha_p \rangle$ and $\langle \Theta_p \rangle_p$.

The pressure gradient term for the fluid phase is defined as

$$S_{f,\text{pressure},i} = -\frac{\partial \langle p_f \rangle}{\partial x_i}, \tag{9}$$

where $\langle p_f \rangle$ is the Reynolds-average fluid-phase pressure. The corresponding particle pressure term applies the particle pressure tensor gradient:

$$S_{p,\text{pressure},i} = -\frac{\partial \rho_p \langle \alpha_p \rangle \langle \mathcal{P}_{p,ij} \rangle_p}{\partial x_j}. \tag{10}$$

The particle pressure momentum transport equation also includes a collisional pressure derived from the Boltzmann-Enskog kinetic theory,

$$S_{p,\text{collision},i} = -\frac{\partial \rho_p \langle \alpha_p \rangle \langle \mathcal{G}_{p,ij} \rangle_p}{\partial x_j}, \tag{11}$$

where

$$\langle \mathcal{G}_{p,ij} \rangle_p = \tfrac{2}{5}(1+e_c)\langle \alpha_p \rangle g_0 (\langle \mathcal{P}_{p,kk} \rangle_p \delta_{ij} + 2\langle \mathcal{P}_{p,ij} \rangle_p) \tag{12}$$

is the collisional pressure tensor [30].

The gravity term for both phases is defined as

$$S_{n,\text{gravity},i} = \rho_n \langle \alpha_n \rangle g_i, \tag{13}$$

where g_i is the gravitational acceleration. Finally, the drag terms for the fluid phase,

$$S_{f,\text{drag},i} = \frac{\rho_p \langle \alpha_p \rangle}{\tau_p}(1-c_g)(\langle u_{p,i} \rangle_p - \langle u_{f,i} \rangle_f), \tag{14}$$

and the particle phase,

$$S_{p,\text{drag},i} = \frac{\rho_p \langle \alpha_p \rangle}{\tau_p}(1-c_g)(\langle u_{f,i} \rangle_f - \langle u_{p,i} \rangle_p), \tag{15}$$

use a Stokes drag model [20], where c_g is the drift velocity correction to the drag coefficient and τ_p is the Stokes particle timescale defined as $\tau_p = d_p^2 \rho_p / (18 \nu_f \rho_f)$.

C. Reynolds stresses

The Reynolds-averaged stress transport equations are defined as

$$\frac{\partial \rho_f \langle \alpha_f \rangle \langle u'''_{f,i} u'''_{f,j} \rangle_f}{\partial t} + \frac{\partial \rho_f \langle \alpha_f \rangle \langle u'''_{f,i} u'''_{f,j} \rangle_f \langle u_{f,k} \rangle_f}{\partial x_k} = S_{f,\text{stress},ij} \tag{16}$$

for the fluid phase and

$$\frac{\partial \rho_p \langle \alpha_p \rangle \langle u''_{p,i} u''_{p,j} \rangle_p}{\partial t} + \frac{\partial \rho_p \langle \alpha_p \rangle \langle u''_{p,i} u''_{p,j} \rangle_p \langle u_{p,k} \rangle_p}{\partial x_k} = S_{p,\text{stress},ij} \tag{17}$$

for the particle phase, where $S_{f,\text{stress},ij}$ and $S_{p,\text{stress},ij}$ are the summed source and sink Reynolds-stress terms for each phase [33,34]. For the fluid phase this sum is defined as

$$\begin{aligned} S_{f,\text{stress},ij} = {} & S_{f,\text{flux},ij} + S_{f,\text{production},ij} + S_{f,\text{pressure-strain},ij} + S_{f,\text{dragstress},ij} \\ & + S_{f,\text{dissipation},ij} + S_{f,\text{interphase},ij} \end{aligned} \tag{18}$$

and the corresponding particle-phase sum is

$$S_{p,\text{stress},ji} = S_{p,\text{flux},ij} + S_{p,\text{production},ij} + S_{p,\text{pressure-strain},ij} + S_{p,\text{dissipation},ij} + S_{p,\text{interphase},ij}. \tag{19}$$

Both phases include terms for spatial flux, turbulent production, pressure-strain redistribution, turbulent dissipation, and interphase coupling. Only the fluid phase has the turbulent drag-stress-production term.

The spatial flux terms include contributions from the diffusive viscous stresses, the triple velocity correlation, and the pressure transport. As done in [19], a gradient-diffusion model is used,

$$S_{f,\text{flux},ij} = \frac{\partial}{\partial x_k} \rho_f \langle \alpha_f \rangle_f \left(\nu_f + \frac{\nu_{f,T}}{\eta_k} \right) \frac{\partial \langle u'''_{f,i} u'''_{f,j} \rangle_f}{\partial x_k}, \tag{20}$$

where η_k is the turbulent viscosity Reynolds-stress coefficient. The particle phase employs the same model for the flux term,

$$S_{p,\text{flux},ij} = \frac{\partial}{\partial x_k} \rho_p \langle \alpha_p \rangle_p \left[\left(\nu_p + \frac{\nu_{p,T}}{\eta_k} \right) \frac{\partial \langle u''_{p,i} u''_{p,j} \rangle_p}{\partial x_k} + \frac{\nu_{p,T}}{\eta_k} \frac{\partial \langle \Theta_p \rangle_p}{\partial x_k} \delta_{ij} \right], \tag{21}$$

and it includes a pressure transport term involving the gradient of the granular temperature. The turbulent viscosity for either phase is defined as the ratio of the squared turbulent kinetic energy, k_n, and the turbulent dissipation,

$$\nu_{n,T} = c_{n,\mu} \frac{k_n^2}{\varepsilon_n}, \tag{22}$$

where $c_{n,\mu}$ is the turbulent viscosity coefficient [20]. The turbulent kinetic energy for both phases are defined as half the trace of their corresponding Reynolds-stress tensor: $k_f = \frac{1}{2} \langle u'''_{f,k} u'''_{f,k} \rangle_f$ for the fluid phase and $k_p = \frac{1}{2} \langle u''_{p,k} u''_{p,k} \rangle_p$ for the particle phase.

The turbulent production term due to mean velocity gradients is defined as

$$S_{f,\text{production},ij} = \rho_f \langle \alpha_f \rangle P_{f,ij} \quad \text{with} \quad P_{f,ij} = -\langle u'''_{f,i} u'''_{f,k} \rangle_f \frac{\partial \langle u_{f,j} \rangle_f}{\partial x_k} - \langle u'''_{f,j} u'''_{f,k} \rangle_f \frac{\partial \langle u_{f,i} \rangle_f}{\partial x_k} \tag{23}$$

for the fluid phase, and

$$S_{p,\text{production},ij} = \rho_p \langle \alpha_p \rangle P_{p,ij} \quad \text{with} \quad P_{p,ij} = -\langle u''_{p,i} u''_{p,k} \rangle_p \frac{\partial \langle u_{p,j} \rangle_p}{\partial x_k} - \langle u''_{p,j} u''_{p,k} \rangle_p \frac{\partial \langle u_{p,i} \rangle_p}{\partial x_k} \tag{24}$$

for the particle phase, where $P_{f,ij}$ and $P_{p,ij}$ are the fluid and particle production tensors due to mean shear.

The Rotta model is used as the basis for the pressure-strain redistribution term for both the fluid and particle phases, with the former including an additional term for the redistribution of drag

production [35]. They are defined as

$$S_{f,\text{pressure}-\text{strain},ij} = -\frac{\rho_f\langle\alpha_f\rangle\varepsilon_f}{k_f}c_{1,f}\left(\langle u'''_{f,i}u'''_{f,j}\rangle_f - \frac{2}{3}k_f\delta_{ij}\right) - \rho_f\langle\alpha_f\rangle c_{2,f}\left(P_{f,ij} - \frac{1}{3}P_{f,kk}\delta_{ij}\right) - \rho_f\langle\alpha_f\rangle c_D\left(P_{g,ij} - \frac{1}{3}P_{g,kk}\delta_{ij}\right) \tag{25}$$

for the fluid phase, and

$$S_{p,\text{pressure}-\text{strain},ij} = \frac{\rho_p\langle\alpha_p\rangle\varepsilon_p}{k_p}c_{1,p}\left(\langle u''_{p,i}u''_{p,j}\rangle_p - \frac{2}{3}k_p\delta_{ij}\right) - \rho_p\langle\alpha_p\rangle c_{2,p}\left(P_{p,ij} - \frac{1}{3}P_{p,kk}\delta_{ij}\right) \tag{26}$$

for the particle phase, where $c_{1,n}$ is the Reynolds-stress redistribution coefficient, $c_{2,n}$ is the stress production redistribution coefficient, and c_D is the drag redistribution coefficient [36]. $P_{g,ij}$ is the turbulent drag production tensor and is defined in the turbulent drag production term [36]

$$S_{f,\text{dragstress},ij} = \rho_p\langle\alpha_p\rangle P_{g,ij} \quad \text{with} \quad P_{g,ij} = \frac{2}{\tau_p}c_g(\langle u_{f,k}\rangle_f - \langle u_{p,k}\rangle_p)^2\delta_{ik}\delta_{jk}. \tag{27}$$

As noted earlier, $P_{g,ij}$ only appears in the fluid phase.

The turbulent dissipation term for the fluid phase,

$$S_{f,\text{dissipation},ij} = -\rho_f\langle\alpha_f\rangle\epsilon_{f,ij} \quad \text{with} \quad \epsilon_{f,ij} = \left(c_f\frac{\langle u'''_{f,i}u'''_{f,j}\rangle_f}{k_f} + \frac{2}{3}(1-c_f)\delta_{ij}\right)\varepsilon_f, \tag{28}$$

and the particle phase,

$$S_{p,\text{dissipation},ij} = -\rho_p\langle\alpha_p\rangle\epsilon_{p,ij} \quad \text{with} \quad \epsilon_{p,ij} = \left(c_p\frac{\langle u''_{p,i}u''_{p,j}\rangle_p}{k_p} + \frac{2}{3}(1-c_p)\delta_{ij}\right)\varepsilon_p, \tag{29}$$

uses a combination of the Rotta turbulent dissipation model and an isotropic turbulence model linked through a blending coefficient c_f for the fluid phase and c_p for the particle phase [31].

The interphase Reynolds-stress coupling term is adapted from the closures in [19] as

$$S_{f,\text{interphase},ij} = \frac{2\rho_p\langle\alpha_p\rangle}{\tau_p}\left(\beta_{fp}\gamma_{sgn,ij}|\langle u'''_{f,i}u'''_{f,j}\rangle_f\langle u''_{p,i}u''_{p,j}\rangle_p|^{1/2} - \beta_f\langle u'''_{f,i}u'''_{f,j}\rangle_f\right) \tag{30}$$

in the fluid phase and

$$S_{p,\text{interphase},ij} = \frac{2\rho_p\langle\alpha_p\rangle}{\tau_p}\left(\beta_{fp}\gamma_{sgn,ij}|\langle u'''_{f,i}u'''_{f,j}\rangle_f\langle u''_{p,i}u''_{p,j}\rangle_p|^{1/2} - \langle u'''_{p,i}u'''_{p,j}\rangle_p\right) \tag{31}$$

for the particle phase, where β_{fp} and β_f are interphase coupling coefficients. $\gamma_{sgn,ij}$ is a sign control coefficient for the asymmetric stresses, defined as

$$\gamma_{sgn,ij} = \begin{cases} \text{sgn}(\langle u'''_{f,i}u'''_{f,j}\rangle_f) & \text{if sgn}(\langle u'''_{f,i}u'''_{f,j}\rangle_f) = \text{sgn}(\langle u''_{p,i}u''_{p,j}\rangle_p), \\ 0 & \text{otherwise.} \end{cases} \tag{32}$$

Note that for the term $|\langle u'''_{f,i}u'''_{f,j}\rangle_f\langle u''_{p,i}u''_{p,j}\rangle_p|$ repeated indices are not summed.

D. Turbulent dissipation rates

The turbulent dissipation transport equation for the fluid and particle phases, respectively, are

$$\frac{\partial\rho_f\langle\alpha_f\rangle\varepsilon_f}{\partial t} + \frac{\partial\rho_f\langle\alpha_f\rangle\varepsilon_f\langle u_{f,i}\rangle_f}{\partial x_i} = S_{f,\text{dissipation}} \tag{33}$$

and

$$\frac{\partial \rho_p \langle \alpha_p \rangle \varepsilon_p}{\partial t} + \frac{\partial \rho_p \langle \alpha_p \rangle \varepsilon_p \langle u_{p,i} \rangle_p}{\partial x_i} = S_{p,\text{dissipation}}, \tag{34}$$

where $S_{f,\text{dissipation}}$ and $S_{p,\text{dissipation}}$ are the dissipation source and sink terms for the fluid and particle phases. The summed dissipation source terms are

$$S_{f,\text{dissipation}} = S_{\varepsilon_f,\text{flux}} + S_{\varepsilon_f,\text{generation}} + S_{\varepsilon_f,\text{destruction}} + S_{\varepsilon_f,\text{interphase}} + S_{\varepsilon_f,\text{drag}} \tag{35}$$

for the fluid phase and

$$S_{p,\text{dissipation}} = S_{\varepsilon_p,\text{flux}} + S_{\varepsilon_p,\text{generation}} + S_{\varepsilon_p,\text{destruction}} + S_{\varepsilon_p,\text{interphase}} \tag{36}$$

for the particle phase. Both phases include terms for turbulent eddy generation and destruction, turbulent diffusive flux, and interphase turbulent dissipation coupling. Only the fluid phase includes a term for turbulent drag dissipation. The turbulent flux term is defined for both phases using an eddy viscosity model as

$$S_{\varepsilon_n,\text{flux}} = \frac{\partial}{\partial x_i} \rho_n \langle \alpha_n \rangle \left(\nu_n + \frac{\nu_{n,T}}{\eta_\varepsilon} \right) \frac{\partial \varepsilon_n}{\partial x_i}, \tag{37}$$

where η_ε is the dissipation turbulent viscosity coefficient that has a nominal value of unity.

The eddy generation and destruction terms for both phases are defined using the Rotta model as

$$S_{\varepsilon_f,\text{generation}} = \frac{\rho_f \langle \alpha_f \rangle \varepsilon_f}{2k_f} c_{\varepsilon 1} P_{f,kk} \tag{38}$$

as the fluid-phase eddy generation term and

$$S_{\varepsilon_f,\text{destruction}} = -\frac{\rho_f \langle \alpha_f \rangle \varepsilon_f}{k_f} c_{\varepsilon 2} \varepsilon_f \tag{39}$$

as the fluid-phase eddy destruction term, where $c_{\varepsilon 1}$ is the eddy generation coefficient and $c_{\varepsilon 2}$ is the eddy destruction coefficient. The corresponding generation and destruction terms are

$$S_{\varepsilon_p,\text{generation}} = \frac{\rho_p \langle \alpha_p \rangle \varepsilon_p}{2k_p} c_{\varepsilon 1} P_{p,kk} \tag{40}$$

and

$$S_{\varepsilon_p,\text{destruction}} = -\frac{\rho_p \langle \alpha_p \rangle \varepsilon_p}{k_p} c_{\varepsilon 2} \varepsilon_p \tag{41}$$

for the particle phase.

The interphase term from [20] used in this model is defined as

$$S_{\varepsilon_f,\text{interphase}} = \frac{2\rho_p \langle \alpha_p \rangle}{\tau_p} c_{\varepsilon 3} (\beta_{fp} \sqrt{\varepsilon_f \varepsilon_p} - \beta_f \varepsilon_f) \tag{42}$$

for the fluid phase and

$$S_{\varepsilon_p,\text{interphase}} = \frac{2\rho_p \langle \alpha_p \rangle}{\tau_p} c_{\varepsilon 3} (\beta_{fp} \sqrt{\varepsilon_f \varepsilon_p} - \varepsilon_p) \tag{43}$$

for the particle phase, where $c_{\varepsilon 3}$ is the interphase dissipation coupling coefficient. The drag dissipation term from [20], used only for the fluid phase, is defined as

$$S_{\varepsilon_f,\text{drag}} = \frac{\rho_p \langle \alpha_p \rangle \varepsilon_p}{k_p} c_{\varepsilon 4} P_{g,kk}, \tag{44}$$

where $c_{\varepsilon 4}$ is the drag dissipation coefficient.

E. Particle pressure tensor

The particle pressure tensor transport equation is found by Reynolds averaging the second-order particle velocity moment transport equation [30] and is defined as [19]

$$\frac{\partial \rho_p \langle \alpha_p \rangle \langle \mathcal{P}_{p,ij} \rangle_p}{\partial t} + \frac{\partial \rho_p \langle \alpha_p \rangle \langle \mathcal{P}_{p,ij} \rangle_p \langle u_{p,k} \rangle_p}{\partial x_k} = S_{\boldsymbol{\mathcal{P}},ij}, \tag{45}$$

where the final term represents production due to the dissipation of the particle-phase Reynolds stresses [1]. The term $S_{\boldsymbol{\mathcal{P}},ij}$ is the sum of the spatial flux and the granular temperature source and sink terms. This sum,

$$S_{\boldsymbol{\mathcal{P}},ij} = S_{\boldsymbol{\mathcal{P}},\text{flux},ij} + S_{\boldsymbol{\mathcal{P}},\text{dissipation},ij} + S_{\boldsymbol{\mathcal{P}},\text{generation},ij} + S_{\boldsymbol{\mathcal{P}},\text{collision},ij} + S_{\boldsymbol{\mathcal{P}},\text{interphase},ij}, \tag{46}$$

includes terms representing generation, particle-particle collisions, and interphase dampening. The flux term, which includes the turbulent flux,

$$S_{\boldsymbol{\mathcal{P}},\text{flux},ij} = \frac{\partial}{\partial x_k} \rho_p \langle \alpha_p \rangle \left(\kappa_p + \frac{\nu_{p,T}}{\eta_\Theta} \right) \frac{\partial \langle \mathcal{P}_{p,ij} \rangle_p}{\partial x_k}, \tag{47}$$

is a result of applying a gradient-diffusion model where $\kappa_p = \nu_p / \mathrm{Pr}_p$ is the granular conductivity coefficient. The granular Prandtl number is $\mathrm{Pr}_p = (16 - 11e_c)/(15 - 5e_c)$ [19]. The turbulent Prandtl number η_Θ is order unity [19]. In the turbulence model, κ_p is evaluated using $\langle \alpha_p \rangle$ and $\langle \Theta_p \rangle_p$.

The generation term due to particle-phase velocity gradients is defined as

$$S_{\boldsymbol{\mathcal{P}},\text{generation},ij} = -\rho_p \langle \alpha_p \rangle \left((\langle \mathcal{P}_{p,ik} \rangle_p + \langle \mathcal{G}_{p,ik} \rangle_p) \frac{\partial \langle u_{p,j} \rangle_p}{\partial x_k} + (\langle \mathcal{P}_{p,jk} \rangle_p + \langle \mathcal{G}_{p,jk} \rangle_p) \frac{\partial \langle u_{p,i} \rangle_p}{\partial x_k} \right). \tag{48}$$

The source term of granular energy resulting from the turbulent dissipation of turbulent kinetic energy is defined as

$$S_{\boldsymbol{\mathcal{P}},\text{dissipation},ij} = \rho_p \langle \alpha_p \rangle \epsilon_{p,ij}. \tag{49}$$

$\epsilon_{p,ij}$ is the particle-phase dissipation tensor defined in (29). The term representing particle-particle collisions was developed using a linearized Bhatnagar-Gross-Krook (BGK) inelastic collision model [37],

$$S_{\boldsymbol{\mathcal{P}},\text{collision},ij} = \frac{2\rho_p \langle \alpha_p \rangle}{\tau_c} (\Delta^*_{ij} - \langle \mathcal{P}_{p,ij} \rangle_p), \tag{50}$$

where Δ^*_{ij} is equal to

$$\Delta^*_{ij} = \frac{(1 + e_c)^2}{4} \langle \Theta \rangle_p \delta_{ij} + \frac{(1 - e_c)^2}{4} \langle \mathcal{P}_{p,ij} \rangle_p, \tag{51}$$

and τ_c is the collisional timescale defined as

$$\tau_c = \frac{d_p}{6 \langle \alpha_p \rangle g_0 \left(\frac{\langle \Theta_p \rangle_p}{\pi} \right)^{1/2}}. \tag{52}$$

Finally, the term representing the interphase dampening of granular energy by the surrounding fluid is defined as

$$S_{\boldsymbol{\mathcal{P}},\text{interphase},ij} = -\frac{2\rho_p \langle \alpha_p \rangle}{\tau_p} \langle \mathcal{P}_{p,ij} \rangle_p. \tag{53}$$

As they should be, all of the terms in (45) are symmetric with respect to indices i and j.

TABLE I. Channel geometrical parameters.

Dimension label	Size (m)
Spanwise (x)	0.054
Wall normal (y)	0.036
Streamwise (z)	0.36
RANS slice streamwise height (z)	0.144

III. SIMULATION AND BOUNDARY CONDITIONS

The geometry used in the simulation cases is a vertical rectangular channel [24,32]. The dimensions of the EE-AG and EL simulations can be seen in Table I. Both EE-AG and EL cases use an identical block grid as the solution mesh, including near-wall refinement based on the work of Kim *et al.* [38]. The RSM model uses a uniform block grid that is close to the refinement of the EE-AG and EL models, but it does not include near-wall refinement. Statistics for the RSM model were collected on a two-dimensional slice on the y-z plane of the same channel. The physical properties of the fluid and particle phases are contained in Table II.

The series of simulation cases done for this study are summarized in Table III. The particle size was varied to execute cases with particles corresponding to a small Stokes number, 1.74, and a large Stokes number, 17.86. The range of mass loadings corresponds to a particle-phase volume fraction of 5×10^{-4} at a mass loading of 0.2 to a volume fraction of 5×10^{-3} at a mass loading of 10 for the large-particle cases. The maximum mass loading for the small-particle case was set at volume fraction of 2×10^{-3} corresponding to a mass loading of 4. Table IV displays the parameters related to the turbulence and particle pressure models contained in this work. The values for the turbulence model parameters are taken from [19]. The values for the Reynolds-stress wall distribution tensor are taken from the documentation for ANSYS Fluent [39].

A. RANS boundary conditions

At the top and bottom of the channel domain, a cyclical periodic boundary is applied for all fields. Flow in the channel is driven by adjusting the fluid-phase pressure gradient in (9) to maintain the mean fluid velocity passing through the inlet and outlet boundary at the value specified in Table II. The wall boundary condition is set as a zero-gradient boundary condition to solve the particle volume fraction continuity equation in (1). Fluid- and particle-phase momentum transport in (2) and (3) use a no-slip and full-slip model for the wall boundary, respectively.

Two different wall models are applied as the boundary condition to the Reynolds-stress transport in (16) and (17), depending on the conditions of the flow. These boundary conditions are based on

TABLE II. Model parameters used in all simulations.

Model parameter	Value
Fluid-phase density ρ_f (kg/m^3)	1
Fluid-phase viscosity ν_f (m^2/s)	1.8×10^{-5}
Overall channel velocity $U_{f,\text{mean}}$ (m/s)	5.02
Pure-fluid channel Reynolds number Re_f	12053
Particle-phase density ρ_p (kg/m^3)	2000
Small particle diameter d_p (μm)	45
Large particle diameter d_p (μm)	144
Particle restitution coefficient e_c	0.9
Gravitational acceleration g_z (m/s^2)	-9.81

TABLE III. Mass-loading cases for each particle size.

Mass loading	$\langle\phi\rangle$
Small particle	0.2, 1, 2, 4
Large particle	0.2, 1, 2, 4, 10

the low-Reynolds-number boundary condition applied in OpenFOAM [40]. For flow conditions for either phase, when the wall boundary layer coordinate

$$y_n^+ = c_{n,\mu}^{1/4} \frac{\Delta_{\text{wall}} k_n^{1/2}}{\nu_n}, \tag{54}$$

where Δ_{wall}, the wall-normal mesh length of the wall cell, is more than the turbulent-laminar threshold value of 11.5, the Reynolds stresses at the walls are defined as

$$\langle u'''_{f,i} u'''_{f,j} \rangle_{f,\,\text{wall}} = -\nu_{f,T\,\text{wall}} \left(\frac{\partial \langle u_{f,i} \rangle_f}{\partial x_j} + \frac{\partial \langle u_{f,j} \rangle_f}{\partial x_i} - \frac{2}{3} \frac{\partial \langle u_{f,k} \rangle_f}{\partial x_k} \delta_{ij} \right) \tag{55}$$

for the fluid phase and

$$\langle u''_{p,i} u''_{p,j} \rangle_{f,\text{wall}} = -\nu_{p,T\,\text{wall}} \left(\frac{\partial \langle u_{p,i} \rangle_p}{\partial x_j} + \frac{\partial \langle u_{p,j} \rangle_p}{\partial x_i} - \frac{2}{3} \frac{\partial \langle u_{p,k} \rangle_p}{\partial x_k} \delta_{ij} \right) \tag{56}$$

TABLE IV. Turbulence and particle pressure model parameters.

Model parameter		Value
Pure-fluid stress redistribution coefficient	c_1	0.6
Pure-fluid production redistribution coefficient	c_2	0.6
Drag redistribution coefficient	c_D	0
Dissipation blending coefficient	c_f	0.93
Dissipation blending coefficient	c_p	0.93
Dissipation generation coefficient	$c_{\varepsilon 1}$	1.44
Dissipation destruction coefficient	$c_{\varepsilon 2}$	1.92
Dissipation interphase coupling coefficient	$c_{\varepsilon 3}$	0.736
Dissipation coefficient	$c_{\varepsilon 4}$	0
Turbulent coupling coefficient	β_f	1.03
Turbulent coupling coefficient	β_{fp}	0.876
Collision coefficient	c_c	2
von Kármán constant	κ	0.41
Wall roughness coefficient	$\mathcal{E}$	9.0
Streamwise Reynolds-stress distribution tensor	$\beta_{w,zz}$	1.098
Wall-normal Reynolds-stress distribution tensor	$\beta_{w,yy}$	0.247
Spanwise Reynolds-stress distribution tensor	$\beta_{w,xx}$	0.655
Shear streamwise/wall-normal Reynolds-stress distribution tensor	$\beta_{w,yz}$	0.255
Shear streamwise/spanwise Reynolds-stress distribution tensor	$\beta_{w,xz}$	0
Shear spanwise/wall-normal Reynolds-stress distribution tensor	$\beta_{w,xy}$	0
Low-Reynolds-number wall parameter	C	11
Specularity factor	ϕ_s	0
Particle-wall restitution coefficient	e_w	1
Wall redistribution coefficient	C_Θ	0

for the particle phase, where $\nu_{f,T\text{wall}}$ and $\nu_{p,T\text{wall}}$ are the fluid and particle-wall turbulent viscosity. The latter is defined for both phases as

$$\nu_{n,T\text{wall}} = \nu_n\left(y_n^+ \frac{\kappa}{\log(\mathcal{E}y_n^+)} - 1\right), \tag{57}$$

where κ is the von Kármán constant and $\mathcal{E}$ is the wall roughness coefficient.

For a flow with the boundary layer coordinate below the turbulent-laminar threshold value of 11.5, the boundary conditions use the solution of the turbulent kinetic energy transport equation for each phase. The fluid-phase turbulent kinetic energy transport equation is defined as

$$\frac{\partial \rho_f \langle\alpha_f\rangle k_f}{\partial t} + \frac{\partial \rho_f \langle\alpha_f\rangle k_f \langle u_{f,k}\rangle_f}{\partial x_k} = S_{f,k}, \tag{58}$$

and the particle-phase turbulent kinetic energy equation is defined as

$$\frac{\partial \rho_p \langle\alpha_p\rangle k_p}{\partial t} + \frac{\partial \rho_p \langle\alpha_p\rangle k_p \langle u_{p,k}\rangle_p}{\partial x_k} = S_{p,k}, \tag{59}$$

where $S_{f,k}$ and $S_{p,k}$ are the summed source and sink terms for the fluid and particle phases. These sums are defined through half the trace of the sum of terms from the corresponding Reynolds-stress transport equation:

$$S_{n,k} = \tfrac{1}{2} S_{n,\text{stress},kk}. \tag{60}$$

The wall boundary condition for the turbulent kinetic energy is defined through the relation

$$k_{n,\text{wall}} = c_{n,\mu}^{1/2} k_n \frac{2400}{c_{\varepsilon 2}^2}\left(\frac{1}{(y_n^+ + C)^2} + 2\frac{y_n^+}{C^3} - \frac{1}{\sqrt{C}}\right), \tag{61}$$

where C is the low-Reynolds-number turbulent kinetic energy fit parameter. This value for the turbulent kinetic energy is related to the Reynolds stresses using constants developed in Gibson and Launder's work modeling near-wall turbulence [41]. In this method, the turbulent kinetic energy at the wall from the boundary condition previously defined is parceled out to each individual Reynolds-stress component:

$$\langle u_{f,i}''' u_{f,j}''' \rangle_{f,\text{wall}} = \gamma_{f,ij} k_{f,\text{wall}}, \quad \langle u_{p,i}'' u_{p,j}'' \rangle_{p,\text{wall}} = \gamma_{p,ij} k_{p,\text{wall}}, \tag{62}$$

where $\gamma_{f,ij}$ and $\gamma_{p,ij}$ are the wall Reynolds-stress distribution tensors for the fluid and particle phases. This tensor must be defined such that $tr(\gamma_{n,ij}) = 2$. For this study, each component of this tensor for both phases is defined as

$$\begin{aligned} \gamma_{n,xx} &= \beta_{w,xx}(1 - \eta_{n,\text{iso}}) & \gamma_{n,xy} &= \beta_{w,xy}, \\ \gamma_{n,yy} &= \beta_{w,yy}(1 - \eta_{n,\text{iso}}) & \gamma_{n,xz} &= \beta_{w,xz}, \\ \gamma_{n,zz} &= \beta_{w,zz}\left(\frac{2 - \beta_{w,zz}}{\beta_{w,zz}}\eta_{n,\text{iso}} + 1\right) & \gamma_{n,yz} &= \beta_{w,yz}, \end{aligned} \tag{63}$$

where $\beta_{w,ij}$ is the wall Reynolds-stress distribution tensor for the fluid phase and $\eta_{n,\text{iso}}$ is an anisotropization factor. At an anisotropization factor value of zero, the stress is distributed at the wall like a pure fluid. At a value of 1, the stress is distributed only to the single streamwise component. This factor can be adjusted between these two values to modulate how Reynolds stress is distributed at the wall.

The boundary conditions for the turbulent dissipation equation at the wall for both phases is defined as

$$\varepsilon_{n,\text{wall}} = c_{n,\mu}^{3/2} \frac{k_n^{3/2}}{\kappa \Delta_{\text{wall}}}. \tag{64}$$

Additionally, the trace of the production for each phase, $P_{n,ii}$, seen in the eddy generation term in (38) and (40) is also modeled at the wall:

$$P_{n,\varepsilon\text{wall},ii} = 2c_{n,\mu}^{1/4}(\nu_n + \nu_{n,T})\left|\frac{\partial\langle u_{n,\text{wall}}\rangle_n}{\partial x_k}\right|\frac{k_n^{1/2}}{\kappa\Delta_{\text{wall}}}, \tag{65}$$

where $\langle u_{n,\text{wall}}\rangle_n$ is the phase-averaged velocity tangential to the wall. It is important to note that the production term near the wall in the Reynolds-stress production terms in (23) and (24) are also modified to make them consistent with the near-wall generation from the turbulent dissipation wall functions:

$$P_{n,\text{wall},ij} = \min\left(\frac{P_{n,\varepsilon\text{wall},ii}}{\text{tr}(P_{n,ij})}, 1\right)P_{n,ij}. \tag{66}$$

Capecelatro *et al.* [19] proposed a wall boundary condition for the granular pressure that is analogous to Johnson-Jackson granular temperature wall boundary conditions. The boundary condition proposed for the diagonal components of the granular pressure tensor is

$$k_\Theta\frac{d\langle\mathcal{P}_{p,\text{wall},ii}\rangle_p}{dx_{\text{wall}-\text{normal}}} = 2\mathcal{D}_w\left(\langle u_{p,i}\rangle_p^2 + \langle u''_{p,i}u''_{p,i}\rangle_p\right) - \mathcal{D}_\Theta\langle\mathcal{P}_{p,ii}\rangle_p - C_\Theta\mathcal{V}_w(\langle\Theta_p\rangle_p - \langle\mathcal{P}_{p,ii}\rangle_p), \tag{67}$$

where $\mathcal{D}_w = \phi_s\mathcal{V}_w$ is a part of a term for granular energy production due to wall slip, $\mathcal{D}_\Theta = -(1-e_w)\mathcal{V}_w$ is a component in a term representing the generation of granular energy due to wall collisions, and C_Θ is a coefficient for the wall granular energy redistribution term. ϕ_s is the specularity factor, and $\mathcal{V}_w$ is the wall collision velocity defined as $\mathcal{V}_w = c_c\pi/6\sqrt{3\langle\Theta_p\rangle_p}$. k_Θ is the granular conductivity coefficient defined as $k_\Theta = \nu_p/\text{Pr}_p$, where $\text{Pr}_p = (16-11e_c)/(15-5e_c)$ is the particle-phase Prandtl number. The boundary condition for the asymmetric y-z component of particle pressure is defined as

$$\langle\mathcal{P}_{p,\text{wall},yz}\rangle_p = \mathcal{D}_w\langle u_{p,z}\rangle_p. \tag{68}$$

Because this work assumes a full-slip boundary condition for the particle-phase velocity, fully elastic particle-wall collisions and no redistribution of granular energy at the wall, the diagonal components of the granular pressure effectively have a zero-gradient boundary condition. Correspondingly, the asymmetric components of the granular pressure tensor have a fixed boundary condition at zero.

B. Simulation solution algorithm

The overall solution algorithm for the model developed in this study is summarized in the following steps:

(1) Initialization of all variables.
(2) Computation of the standard fluid-phase Courant-Friedrichs-Lewy (CFL) condition,

$$C_{\text{CFL},f} = \max\left(\frac{1}{2V}\Delta t\sum_{\text{faces}}|\phi_f|\right), \tag{69}$$

and the interphase CFL condition,

$$C_{\text{CFL,interphase}} = \max\left(\frac{1}{2V}\Delta t\sum_{\text{faces}}|\phi_p - \phi_f|\right), \tag{70}$$

where V is the cell volume, and ϕ_f and ϕ_p are the fluid-phase and particle-phase surface velocity fluxes, respectively. The overall CFL condition, which limits the timestep magnitude, is taken from the maximum of these two conditions,

$$C_{\text{CFL}} = \max(C_{\text{CFL},f}, C_{\text{CFL,interphase}}). \tag{71}$$

(3) Particle-phase fields for volume fraction, $\langle \alpha_p \rangle$, velocity, $\langle u_{p,i} \rangle_p$, Reynolds stress, $\langle u''_{p,i} u''_{p,j} \rangle_p$, dissipation, ε_p, and particle pressure, $\langle \mathcal{P}_{ij} \rangle_p$ are updated using their corresponding equations in (1), (3), (17), (34), and (45), respectively.

(4) Fluid-phase fields for Reynolds stress, $\langle u'''_{f,i} u'''_{f,j} \rangle_f$, and dissipation, ε_f, are updated using their corresponding equations in (2) and (33), respectively.

(5) The fluid-phase momentum transport equation from (2), $\langle u_{f,i} \rangle_f$, is constructed as a semidiscretized equation separating diagonal and off-diagonal elements,

$$\langle u_{f,i} \rangle_f = \lambda_f (\mathbb{H} + \rho_f \langle \alpha_f \rangle g_i + K_{\text{drag}} \langle u_{p,i} \rangle_p - \nabla \mathcal{P}_f), \tag{72}$$

where $\lambda_f = (\mathbb{A} + K_{\text{drag}})^{-1}$ is the inverse of the sum of the diagonal coefficients $\mathbb{A}$ and the overall drag coefficient $K_{\text{drag}} = \phi(1 - c_g)/\tau_p$ and $\mathbb{H}$ represents the off-diagonal contributions to the fluid-phase equation.

(6) The fluid-phase pressure-gradient equation constructed using the fluid-phase velocity fluxes on each cell surface $\mathbf{S}$,

$$\begin{aligned}(\langle \alpha_f \rangle \lambda_f)_{\text{face}} |\mathbf{S}| \nabla^{\perp} \mathcal{P}_f = {} & \frac{d\alpha_f}{dt} + \langle \alpha_{f,\text{face}} \rangle ((\lambda_f \mathbb{H})_{\text{face}} \cdot \mathbf{S} + \lambda_{f,\text{face}} \rho_f \langle \alpha_{f,\text{face}} \rangle \mathbf{g} \cdot \mathbf{S} \\ & + \lambda_{f,\text{face}} (K_{\text{drag}} \langle u_p \rangle_p)_{\text{face}} \cdot \mathbf{S}),\end{aligned} \tag{73}$$

develops the fluid-phase pressure field and its result is applied to update the fluid-phase velocity field.

(7) Iterate steps 5 through 6 until the fluid-phase pressure converges.

(8) Advance in time and repeat from step 2 until the solution is complete.

IV. RESULTS AND DISCUSSION

In this section, results from the RSM are compared to predictions of EL and EE-AG simulations for vertical channel flow with and without particles. First, however, an *a priori* analysis of the EL data is employed to fit key parameters in the RSM as a function of the mass loading.

A. Parameter specification

Several parameters appearing in the RSM must be extracted from EL turbulence statistics to determine how they change as the mass loading $\langle \phi \rangle$ increases. Three sets of parameters were focused on for modification in this model: the drag coefficient, the wall anisotropization factor, and the pressure-strain redistribution coefficients.

The drag coefficient parameter c_g present in the interphase drag exchange term in (14) and (15) and the drag production term in (27) is directly computed from the EL data. Unlike in our previous work [19], for simplicity here we do not make c_g a function of the distance from the channel wall. Figure 1 shows the drag coefficient as a function of the mass loading using both the small and large particles. The constant drag coefficient is computed from the EL results as a constant computed from averaging over the volume of channel. In both cases the drag coefficient increases with the mass loading, and with the small particles it increases more gradually. Based on the results in our prior work [19], the drift velocity (and hence c_g) is very small near the channel wall. Thus we can expect that using the channel-average value for c_g is likely to overpredict the kinetic energy near the wall.

The anisotropization factor for the Reynolds-stress wall boundary condition in (63), $\eta_{n,\text{iso}}$, is taken directly from the values of the Reynolds stresses at the wall averaged over the channel in the EL results for both phases. This value as a function of the mass loading for the small and large particles can be seen in Fig. 2. As the mass loading increases, so does the fluid-phase anisotropy at the wall. The anisotropy of the particle phase, on the other hand, at the wall remains consistently highly anisotropic at all mass loadings.

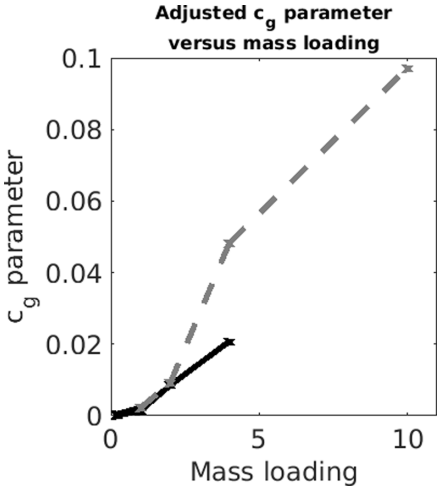

FIG. 1. EL average c_g as a function of mass loading $\langle\phi\rangle$ using small (▬) and large (▬ ▬) particles.

The parameters $c_{1,n}$ and $c_{2,n}$ used in the pressure-strain redistribution tensor in (25) and (26) were also modified in a similar way based on the anisotropy seen in the stresses extracted from the EL model for each phase for the entire wall-normal profile rather than just at the wall. Figure 3 shows how the parameters were modified for the fluid and particle phase using each particle size. Through an initial comparison with the pure-fluid EL model case, a value of 0.6 was chosen as the baseline for both $c_{1,n}$ and $c_{2,n}$. These constants were reduced up to a baseline of 0.18 to match the degree of anisotropization observed in the EL model at each mass loading. The particle phase consistently had a high degree of anisotropization, even at the smallest mass loadings. The only difference between the large and small particles was that the larger particles had less anisotropization at higher mass loadings than the small particles.

Using the parameters found above, in the following sections time-averaged statistics collected from the EL and EE-AG simulations are compared with their counterparts obtained using the RSM model.

B. Vertical channel flow without particles

For the pure-fluid case, Fig. 4 shows the velocity, Reynolds stresses, and turbulent kinetic energy for all three simulations. The profiles for all models in this and all subsequent figures in this work

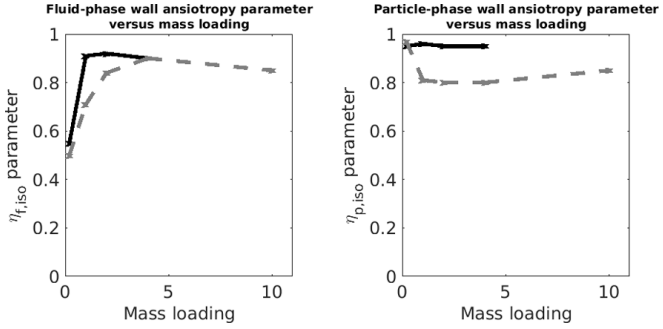

FIG. 2. EL average fluid-phase and particle-phase ansiotropization factor as a function of mass loading $\langle\phi\rangle$ using small (▬) and large (▬ ▬) particles.

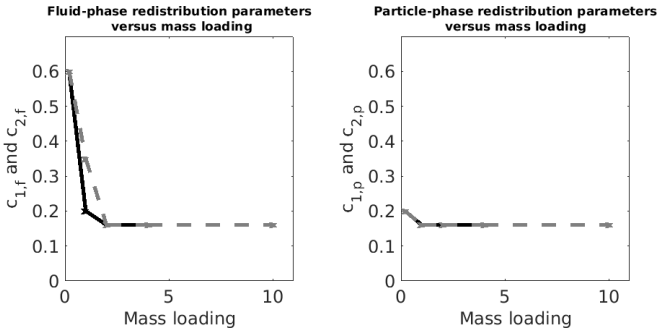

FIG. 3. Fluid-phase and particle-phase Reynolds stress and redistribution coefficients based on EL data using small (▬) and large (▬ ▬) particles.

are generated through averaging down the length of the channel over 1 s of flow time. The phase velocity is normalized using the channel velocity from Table II, and the Reynolds stresses are normalized using the corresponding turbulent kinetic energy of the phase. The turbulent kinetic energy is normalized using the square of the channel velocity. Both the EL and EE-AG models solve the same equations on the same grid, so any differences are a result of the numerical discretization.

The mean fluid velocity for the RSM shows excellent correspondence with the other models. Towards the center of the channel, the RSM shows good correspondence with the Reynolds stresses in the other models. One feature seen in the EL and EE-AG models that is not resolved in the RSM is the peak of high anisotropy in the streamwise component near the walls. Additionally, the overall fluid-phase turbulent kinetic energy decreases at a slower rate from the peak in the near-wall region. One reason for this deviation in the near-wall region can be observed in Fig. 5, where the RSM overpredicts the turbulent production in the streamwise direction in the near-wall region. This appears to be a product of transitioning to low-Reynolds-number behavior as the wall is approached from the channel center, which is not accounted for in the RSM.

From a purely computational standpoint, the same grid is used in the EL and EE-AG codes but with different-order numerics (higher in EL than EE-AG). Thus the EL results can be taken as the reference solution for all cases. As a general rule, the accuracy of the predictions from the RSM for particle-laden cases cannot be expected to be better than for the pure-fluid case.

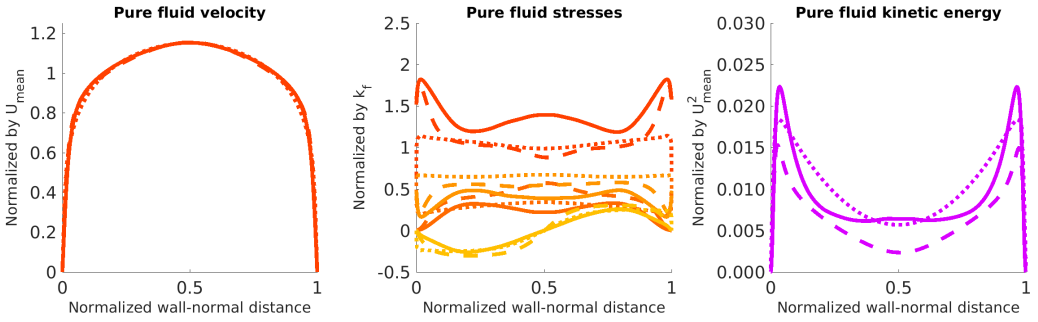

FIG. 4. Pure-fluid case comparison of EE-AG, EL, and RSM data. Streamwise components (z or zz) for the EE-AG, EL, and RSM cases are respectively denoted as (▬), (▬ ▬), and (▪▪▪▪); wall-normal components (yy) as (▬),(▬ ▬), and (▪▪▪▪); spanwise components (xx) as (▬), (▬ ▬), and (▪▪▪▪); and shear components (yz) as (▬), (▬ ▬), and (▪▪▪▪). Fluid-phase turbulent kinetic energy is denoted as (▬), (▬ ▬), and (▪▪▪▪).

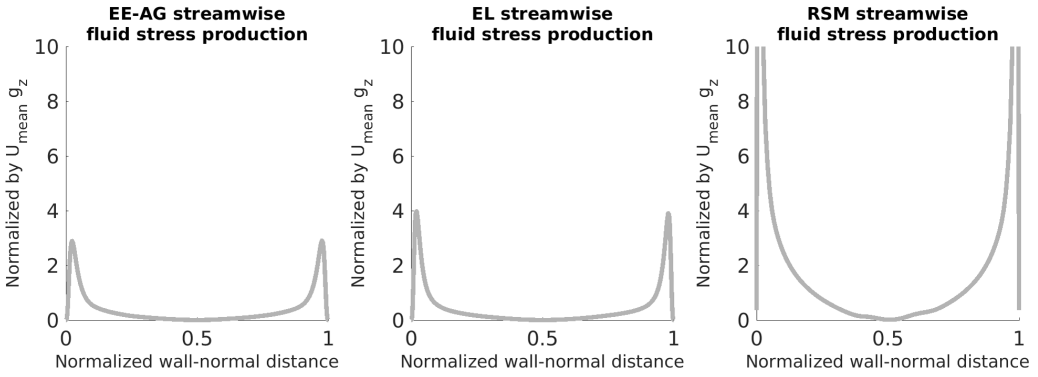

FIG. 5. Pure-fluid streamwise production term comparison.

C. Vertical channel flow with particles

Unlike in the pure-fluid case, the continuity equation for the particle volume fraction plays an important role in particle-laden flows. While it is often assumed in RANS modeling studies [42] that the Reynolds-average volume fraction is time independent in fully developed particle-laden channel flows, this is not the case due to the hyperbolic nature of the particle-phase governing equations. Thus, as shown in Fig. 6, the instantaneous RSM fields for small particles exhibit clustering much like that seen in EE-AG. In comparison, for larger particles as shown in Fig. 7, clustering is less pronounced in the RSM. Nonetheless, the ability to predict the particle-phase volume fraction distribution is a significant challenge in the RSM context.

When examining the time-average particle distribution over the width of the channel for the small particles in Fig. 8(a), preferential channeling of the particle phase towards the center of the channel that does not appear in either the EE-AG or EL models occurs for all except the largest mass loading. Because the RSM inherently dampens turbulent instabilities in the channel, the primary means of the wall-normal transport of particles come from the gradient of the particle-phase Reynolds stress seen in (3) or the particle pressure through the particle pressure gradient in (10) and the gradient of the collisional flux in (12). The drag term in (15) also plays an important role in the distribution of the particle phase through the increase of its magnitude in areas of high particle concentration. The reason why these high particle concentrations are sustained at the center of the channel in these cases is due to how the gradients of the Reynolds stresses and particle pressure are weakest there. The greater particle velocity at the wall compared with the other models makes it easier for the

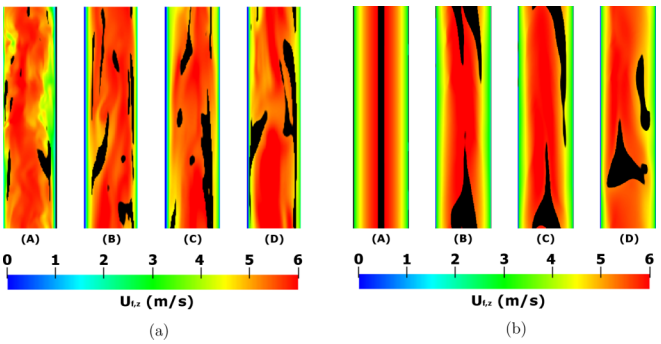

FIG. 6. Instantaneous velocity of the (a) EE-AG and (b) RSM with cells with particle volume fraction greater than 1.75 $\alpha_{p,\mathrm{mean}}$ superimposed at mass loadings $\langle\phi\rangle$ of (A) 0.2, (B) 1, (C) 2, and (D) 4 with small particles.

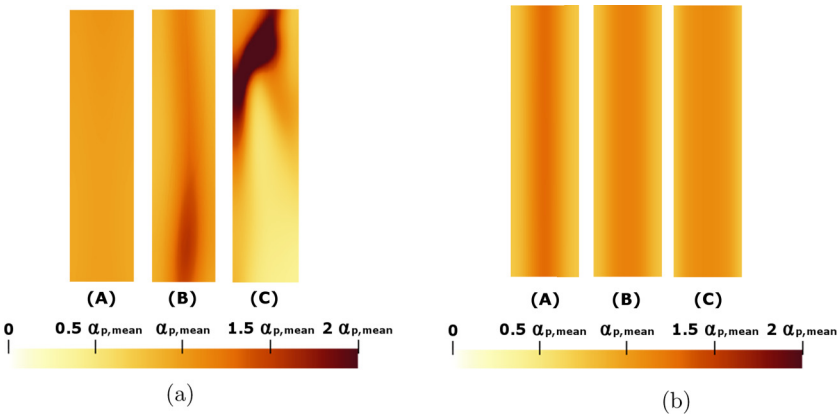

FIG. 7. Instantaneous volume fraction of the (a) EE-AG model and (b) RSM at mass loadings $\langle\phi\rangle$ of (A) 2, (B) 4, and (C) 10 with large particles.

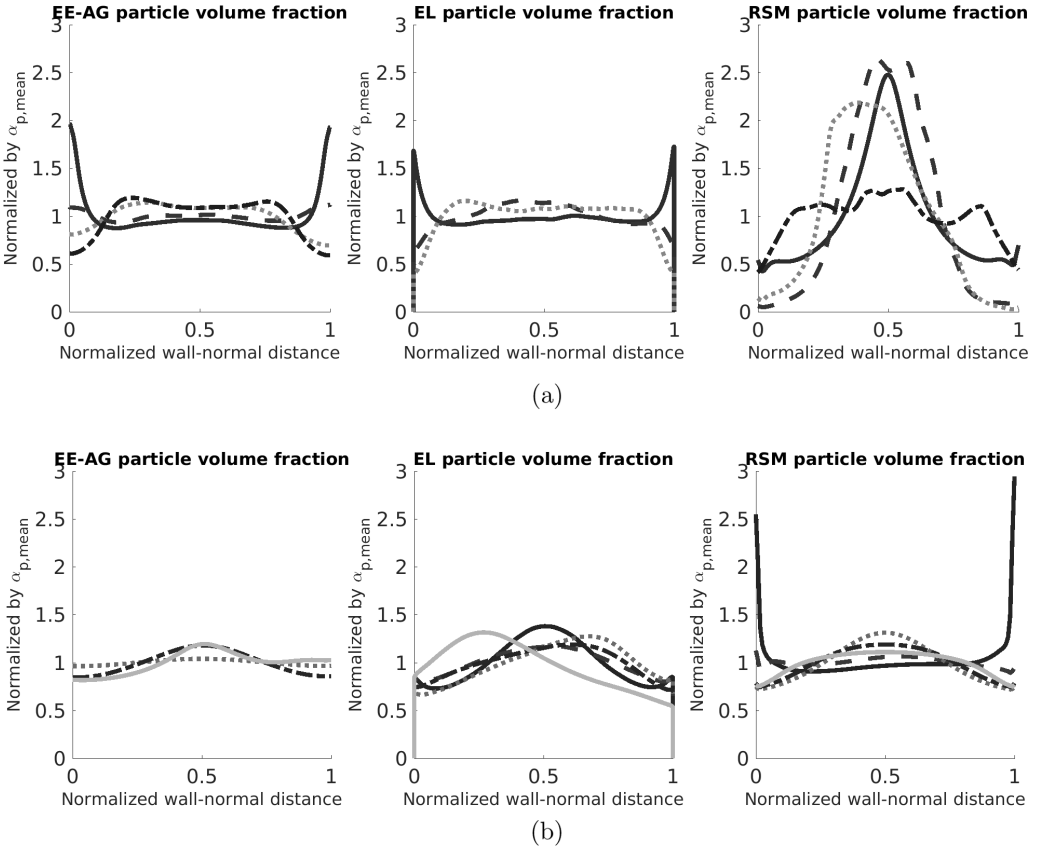

FIG. 8. Time-average particle-phase volume fraction profiles. ML = 0.2 cases are denoted as (——), ML = 1 cases are denoted as (– –), ML = 2 cases are denoted as (·····), ML = 4 cases are denoted as (– – –), and ML = 10 cases are denoted as (——). (a) Small particles and (b) Large particles.

particle phase to move away from the wall to get trapped in the center. The RSM also demonstrates an increase in the granular energy in the approach to the wall, which causes the repulsion of particles away from it. This increase was matched by the EL results but is absent in the EE-AG results. RSM for the mass loading of 4 compares well with the EE-AG result. The overall decrease in particle-phase kinetic energy as well as a smaller granular pressure gradient make it so that the particles are no longer trapped in the center of the channel.

The time-average particle distribution of the large-particle case in Fig. 8(b) shows reasonably good agreement between the EL and the RSM data in all cases but the most dilute one. In that case, the particle phase was uniform in the center of the channel but showed accumulation at the walls, not unlike what is observed in the most dilute EL case using smaller particles in Fig. 8(a) (see also [11]). As discussed below, in all of these cases the particle-phase turbulence and granular energy is relatively small and uniform. The increased decoupling from the fluid phase with the greater Stokes timescale associated with larger particles in (15) and (31) means that less of the fluid-phase momentum and turbulence is being transferred to the particle phase. This lack of significant turbulence in the particle phase correspondingly creates a particle distribution that is absent of clustering down the length of the channel, in contrast with the small-particle cases.

The time-average fluid-phase velocities, kinetic energy, and Reynolds stresses of the EL, EE-AG, and RSM simulations with small particles can be seen in Fig. 9. The EL mass loading of 4 case is omitted here due to a parameter error resulting in a slower mean channel velocity. The same profiles for the cases using large particles can be seen in Fig. 10. The low-mass-loading cases with large particles corresponding to a mass loading of 0.2, 1, and 2 using the EE-AG model are also omitted due their extremely small particle number density. The EE-AG model does not accurately capture the behavior of spatially intermittent systems such as these [32].

Overall, the RSM fluid-phase velocity profiles show reasonably good agreement with the EE-AG and EL models, with the RSM consistently slightly underpredicting the slope as the profile begins to level off going away from the wall. For the highest-mass-loading case using large particles in Fig. 10(e), the RSM demonstrates the flattening of the fluid-velocity profile seen in the EE-AG and EL simulations. Remarkably, the relatively poorer RSM predictions for the particle volume fraction do not have a significant effect on the velocity profiles.

For both particle sizes and at all mass loadings, the RSM significantly overpredicts the fluid-phase turbulent kinetic energy versus the other simulations near the wall. The largest contributor to this overprediction of fluid-phase Reynolds stress comes from the use of a uniform drag coefficient. This causes the drag-stress-production term in (27) to be at its largest value closest to the wall when the difference between the fluid and particle velocities is correspondingly at its largest value. This results in a significant amount of fluid-phase turbulent kinetic energy to be applied to the system near the wall. Additionally, as observed in the pure-fluid-phase case in Fig. 5, the RSM inherently overpredicts the fluid-phase turbulent production close to the wall. Despite this issue, the RSM does come closer to matching the fluid-phase turbulent kinetic energy of other models towards the center of the channel. Away from the walls, the RSM demonstrates the initial collapse in the fluid-phase turbulent kinetic energy for both particle sizes as the mass loading is increased from the most dilute case. For the large-mass-loading cases using the large particles in Figs. 10(d) and 10(e), the RSM also shows the same recovery of the fluid-phase turbulent kinetic energy following this collapse observed in the other models.

The anisotropy of the RSM fluid-phase Reynolds stresses shows good agreement with the other models in the lower-mass-loading cases in Figs. 9 and 10(a) and 10(b). As in the pure-fluid case, the RSM does not resolve the near-wall high-anisotropy peak for these cases and generally underpredicts the anisotropy close to the wall at higher mass loadings as well. For both the small- and large-particle cases, the RSM demonstrates the same increase in anisotropy with increased mass loading as observed in the EL and EE-AG simulations. The anisotropy of the RSM matches well with the other simulations at higher mass loadings for the small particles. The large-particle intermediate-mass-loading RSM case in Fig. 10(c) slightly underpredicts the anisotropy of the other simulations, but the subsequent high-Stokes cases in Figs. 10(d) and 10(e) match them at the center

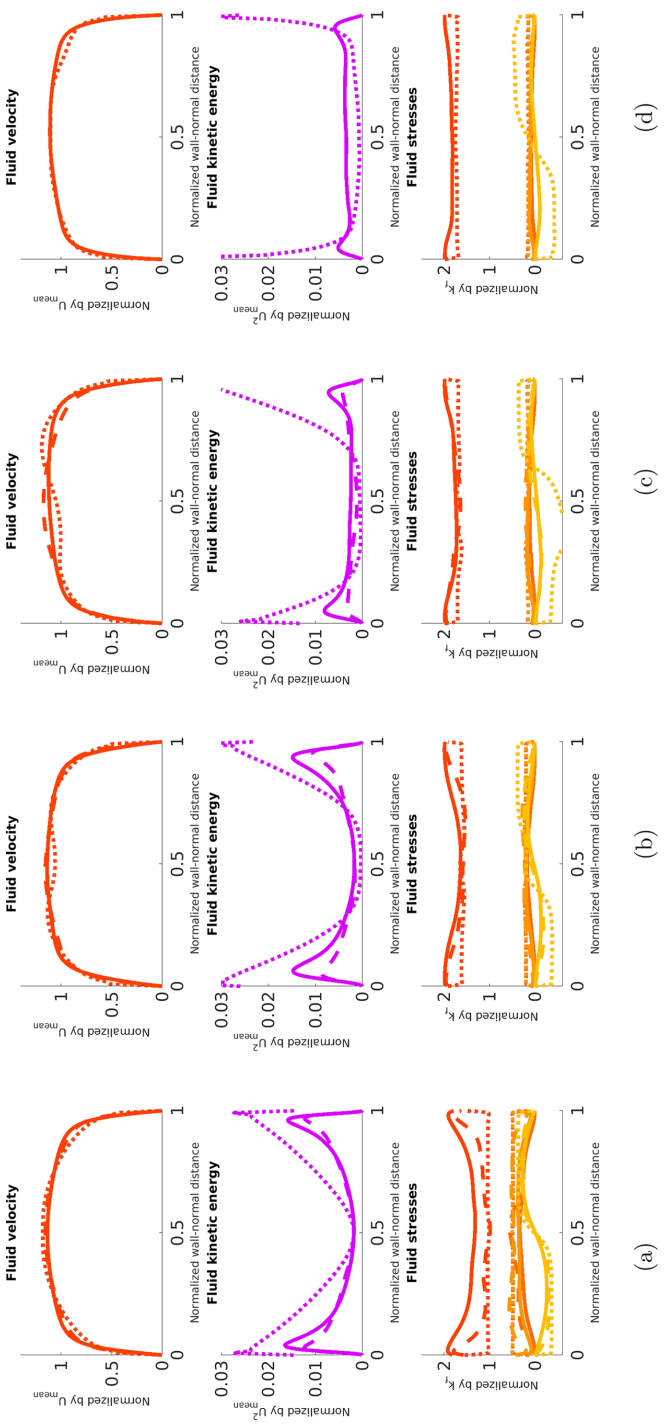

FIG. 9. Fluid-phase velocity and stress comparisons for small particles. Streamwise components (z or zz) for the EE-AG, EL, and RSM cases are denoted, respectively, as (——), (– –), and (····); wall-normal components (yy) as (——),(– –), and (····); spanwise components (xx) as (——), (– –), and (····); and shear components (yz) as (——), (– –), and (····). Fluid-phase turbulent kinetic energy is denoted as (——), (– –), and (····). (a) $\langle\phi\rangle = 0.2$, (b) $\langle\phi\rangle = 1$, (c) $\langle\phi\rangle = 2$, and (d) $\langle\phi\rangle = 4$.

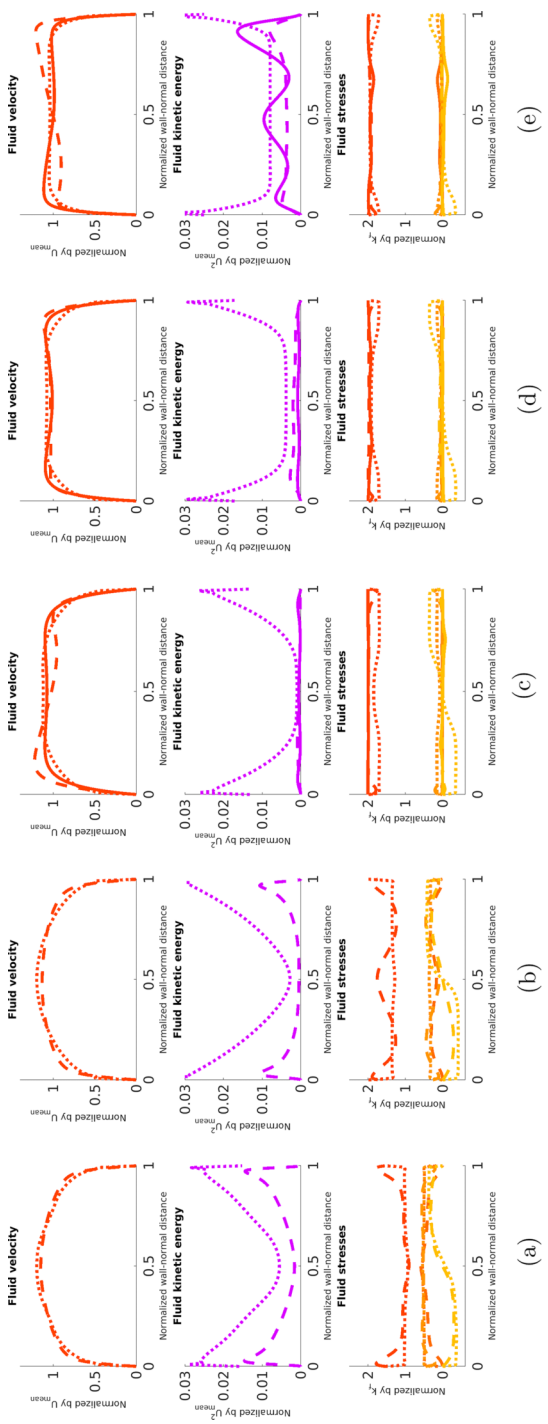

FIG. 10. Fluid-phase velocity and stress comparisons for large particles. Streamwise components (z or zz) for the EE-AG, EL, and RSM cases are denoted, respectively, as (——), (– –), and (····); wall-normal components (yy) as (——),(– –), and (····); spanwise components (xx) as (——), (– –), and (····); and shear components (yz) as (——), (– –), and (····). Fluid-phase turbulent kinetic energy is denoted as (——), (– –), and (····). (a) $\langle\phi\rangle = 0.2$, (b) $\langle\phi\rangle = 1$, (c) $\langle\phi\rangle = 2$, (d) $\langle\phi\rangle = 4$, and (e) $\langle\phi\rangle = 10$.

of the channel. Both the EE-AG and EL simulations demonstrate a collapse in the shear stress as the mass loading increases for both large and small particles that only begins to happen in the large-particle case at the center of the channel at the largest mass loading in Figs. 10(d) and 10(e).

The corresponding time-average particle-phase profiles of the streamwise velocity, kinetic energy, Reynolds stresses, and particle pressure are seen in Fig. 11 for the small particles and Fig. 12 for the large particles. While the RSM particle-phase velocity profiles show good agreement with the EE-AG and EL simulations for both particle sizes, there exists a deviation in the particle-phase velocity close to the wall for the small-particle cases. In those cases, the RSM consistently overpredicts the particle-phase velocity close to the wall. The particle-phase turbulent kinetic energy and fluctuating kinetic energy show reasonably good agreement between all three models, with the exception of the dilute small-particle cases seen in Figs. 11(a) and 11(b), where agreement is lacking between the EE-AG and EL models. All models demonstrate the overall decline in both the particle-phase turbulent kinetic energy and fluctuating kinetic energy as the mass loading is increased. The anisotropy of the particle stresses and granular pressure generally showed good agreement between all models. For all cases, sizes, and models, the anisotropy was consistently large for the particle-phase Reynolds stresses. For the particle pressure, the RSM was able to capture the overall decline in anisotropy as the mass loading was increased that was observed in the other models.

One important phenomena observed in both the EL and EE-AG simulations is a transition in fluid-phase turbulence as the mass loading increases. At more dilute concentrations of particles, the fluid-phase turbulence behaves much as it does in the pure-fluid case. As more particles are added, interphase coupling causes more and more of the fluid turbulent kinetic energy to be drained away, resulting in the turbulence of the fluid phase to enter a relaminarized state. As even more particles are added, they form clusters that begin to generate turbulence in the fluid phase, causing the turbulence of the system to enter a CIT regime. Figure 6(a) demonstrates this entire transition through superimposing the cells with a particle volume fraction greater than $1.75\alpha_p$ on the instantaneous streamwise fluid-phase velocity. Figure 6(a) panel (A) shows how the turbulent instabilities fade as more particles are added at a mass loading of 1 and 2 in (B) and (C). At the largest mass loading in (D), the fluid velocity carves a path around the areas of large particle concentration, demonstrating CIT.

For the RSM cases in Fig. 6(b), evidence of CIT can be observed at larger mass loadings for small particles. For the small particles in Fig. 6(b) panel (D) and to a lesser extent in (C), the fluid-phase streamwise velocity carves itself around the large concentrations of particles. Likewise, for the large particles in Fig. 7(b) panels (D) and (E), the fluid velocity weaves itself around the more singular large-particle concentration. Unlike what was observed in the EE-AG large-particle cases, the direct formation of fluid-phase turbulent instabilities that are not present for the RSM in Figs. 6(b) and 7(b) is instead prevented by design through the implementation of the turbulence model. Unlike the small-particle cases, the RSM did not develop the same instantaneous clustering using large particles and thus evidence of CIT cannot be identified in the instantaneous profiles in the same way. In the EE-AG model in Fig. 7(a), only a single large cluster has developed at the largest mass loading. Instead, as seen in Fig. 7(b), the RSM particle profile is nearly uniform over the length of the channel for all cases.

The streamwise fluid-phase Reynolds-stress profiles for the small-particle cases in Fig. 13(a) and the large-particle cases in Fig. 13(b) both show a collapse in the fluid-phase turbulence as more particles are added starting from the pure-fluid phase for the RSM, the EE-AG, and the EL simulations where there are data available. However, this collapse is not observed in the RSM in the near-wall region, which remains at a consistently large magnitude for all mass loadings. Additionally, while the small-particle EE-AG and EL cases show a recovery in fluid-phase turbulence from CIT at the largest mass loadings, the same is not true for the RSM. For the large-particle case, on the other hand, there is an increase in the fluid-phase turbulence in the center of the channel at the two highest mass loadings using the RSM in line with the EE-AG and EL results.

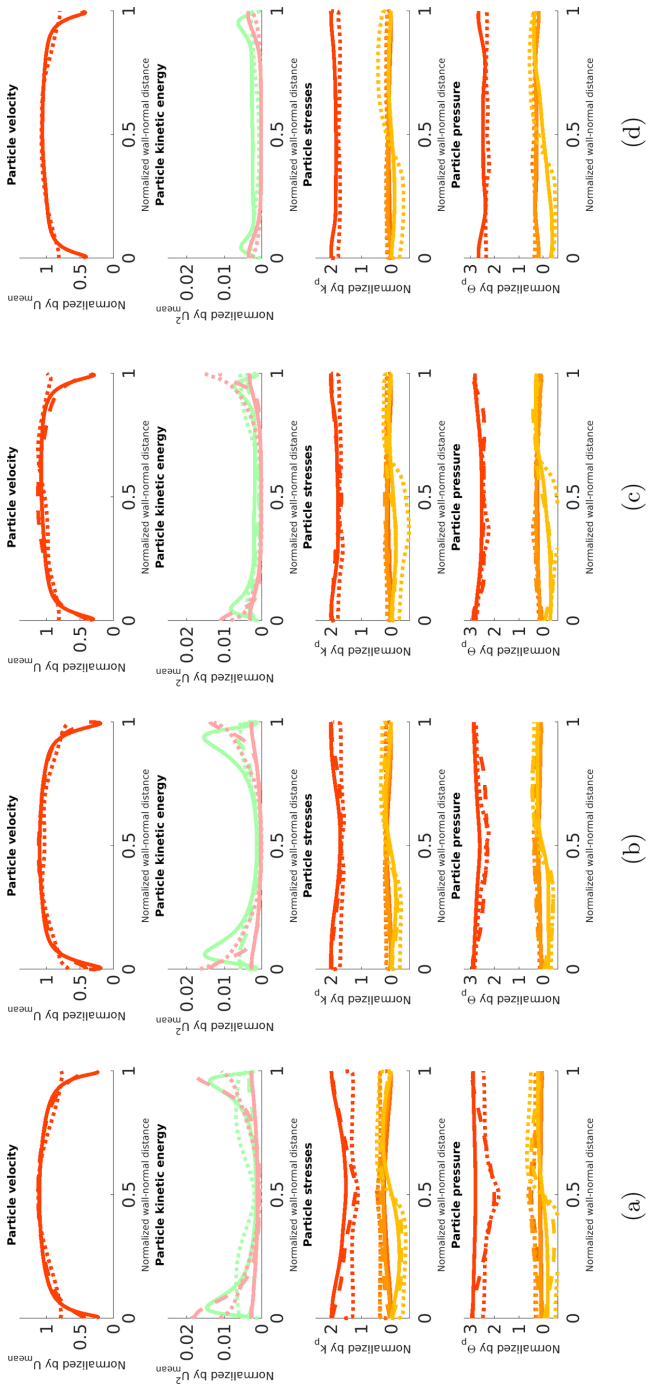

FIG. 11. Particle-phase velocity, stress, and pressure comparisons for small particles. Streamwise components (z or zz) for the EE-AG, EL, and RSM cases are denoted, respectively, as (▬), (▬ ▬), and (▪▪▪▪); wall-normal components (yy) as (▬),(▬ ▬), and (▪▪▪▪); spanwise components (xx) as (▬), (▬ ▬), and (▪▪▪▪); and shear components (yz) as (▬), (▬ ▬), and (▪▪▪▪). Correlated particle-phase turbulent kinetic energy is denoted as (▬), (▬ ▬), and (▪▪▪▪) and uncorrelated particle-phase fluctuating kinetic energy as (▬), (▬ ▬), and (▪▪▪▪). (a) $\langle\phi\rangle = 0.2$, (b) $\langle\phi\rangle = 1$, (c) $\langle\phi\rangle = 2$, and (d) $\langle\phi\rangle = 4$.

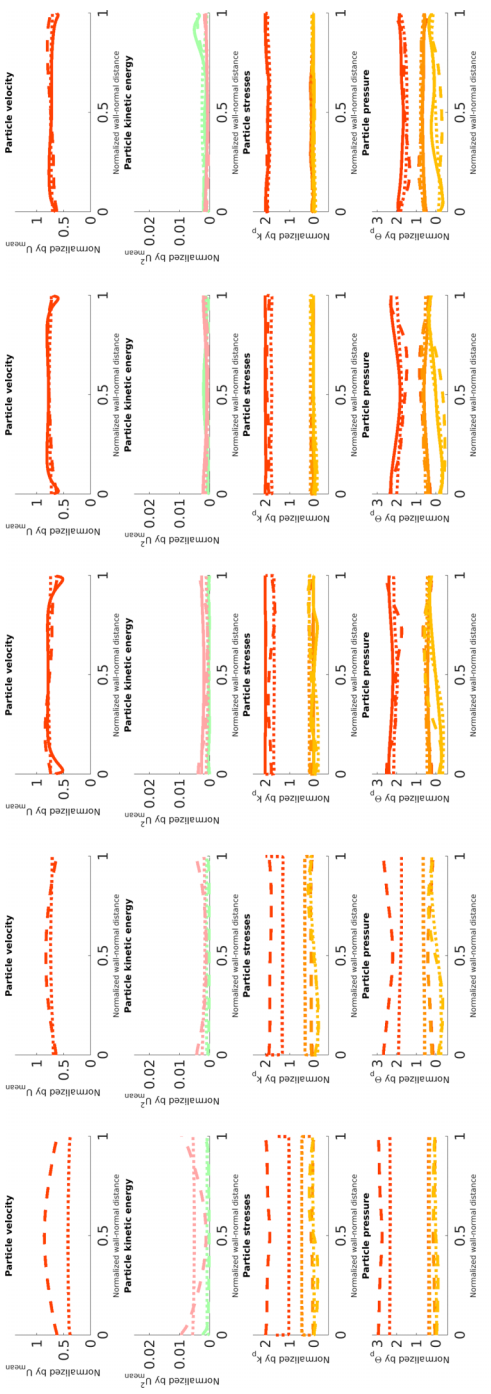

FIG. 12. Particle-phase velocity, stress, and pressure comparisons for large particles. Streamwise components (z or zz) for the EE-AG, EL, and RSM cases are denoted, respectively, as (▬), (▬ ▬), and (▬ ▪ ▬ ▪); wall-normal components (yy) as (▬),(▬ ▬), and (▬ ▪ ▬ ▪); spanwise components (xx) as (▬), (▬ ▬), and (▬ ▪ ▬ ▪); and shear components (yz) as (▬), (▬ ▬), and (▬ ▪ ▬ ▪). Correlated particle-phase turbulent kinetic energy is denoted as (▬), (▬ ▬), and (▬ ▪ ▬ ▪) and uncorrelated particle-phase fluctuating kinetic energy as (▬), (▬ ▬), and (▬ ▪ ▬ ▪). (a) $\langle\phi\rangle = 0.2$, (b) $\langle\phi\rangle = 1$, (c) $\langle\phi\rangle = 2$, (d) $\langle\phi\rangle = 4$, and (e) $\langle\phi\rangle = 10$.

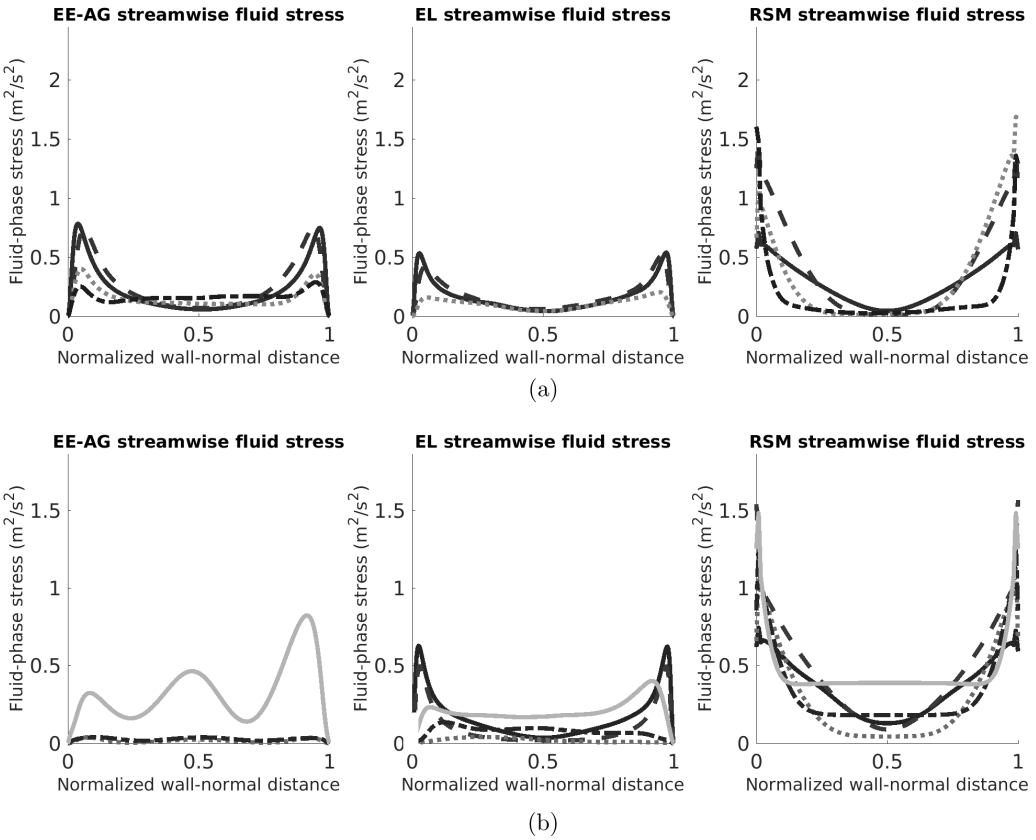

FIG. 13. Fluid-phase streamwise Reynolds-stress profile. ML=0.2 cases are denoted as (▬▬), ML=1 cases are denoted as (▬ ▬), ML=2 cases are denoted as (▪▪▪▪▪), ML=4 cases are denoted as (▬ ▪ ▬), and ML=10 cases are denoted as (▬▬). (a) Small particles and (b) Large particles.

The reason for these differences in the behavior of the RSM and the other models can be seen when examining the turbulent-stress-production term from (23) and the drag-production term from (27) for the streamwise fluid-phase Reynolds stress extracted from all three models in Figs. 14 and 15. For the EL and EE-AG models, the fluid-phase turbulent production collapses as more particles, large or small, are added. While the fluid-phase turbulent production erodes as more particles are added, there is no significant decline in the near-wall region for the RSM. For the small particles, the RSM model significantly underpredicts the turbulent drag production. This smaller drag term explains the lack of a rebound in fluid-phase turbulence in Fig. 13(a) at the highest mass loadings. The large-particle RSM cases, on the other hand, have a drag-production term that corresponds to an increase in fluid-phase turbulence after relaminarization at the center of the channel in Fig. 13(b). This is evidence of the impact of CIT. Having a large enough drag-production term also caused the large particles to show a high degree of anisotropy at the center of the channel for the RSM that matched the EE-AG and EL simulations in Figs. 10(d) and 10(e).

V. CONCLUSIONS

In this work, a transient Reynolds-stress model using Reynolds-averaged transport equations for both phases was implemented to describe particle-laden vertical channel flow. Fluid-phase turbulence and correlated particle-phase turbulence were captured using a RSM. Uncorrelated

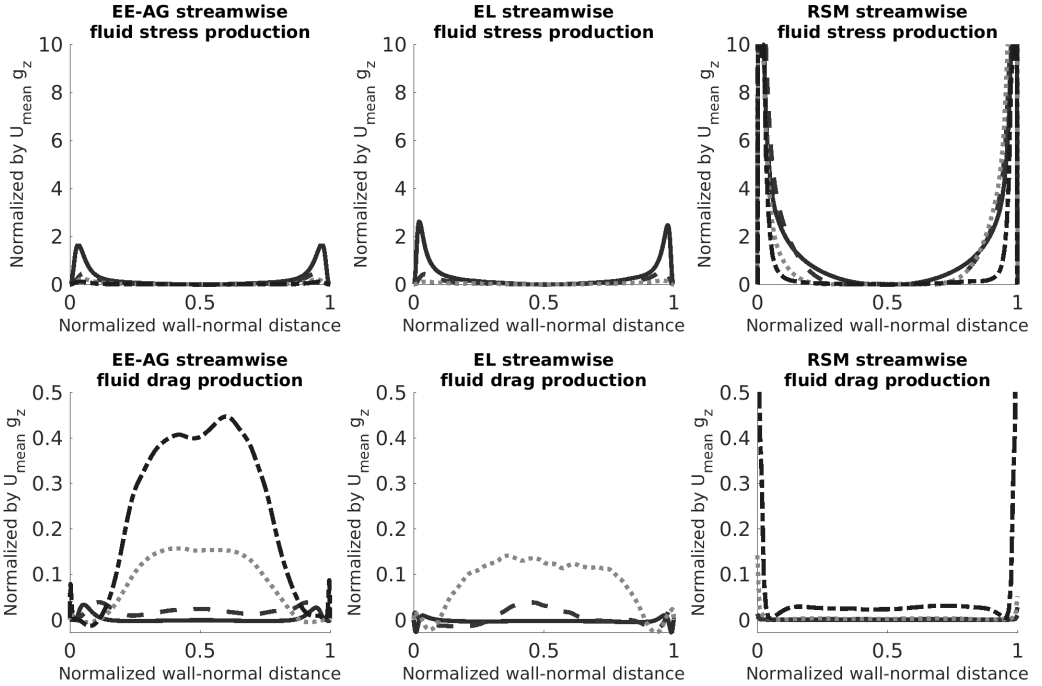

FIG. 14. Fluid-phase streamwise Reynolds-stress turbulent-production and drag-production terms with small particles. ML = 0.2 cases are denoted as (▬▬), ML = 1 cases are denoted as (▬ ▬), ML = 2 cases are denoted as (▪▪▪▪▪), and ML = 4 cases are denoted as (▬ ▪ ▬).

particle-phase fluctuating kinetic energy was captured using a Reynolds-averaged anisotropic particle pressure model based on the kinetic theory of granular flow. EL data from this channel were used to inform the RSM closures and parameters relating to the drag coefficient and the redistribution of turbulent kinetic energy for both phases. Two sets of cases were done for a range of mass loadings for small or large particles. The RSM was able to capture fluid and particle velocity profiles similar to the EL and EE-AG models for both large and small particles and at all mass loadings. The RSM features the same flattening of the fluid and particle velocity profile as more particles are added. While the RSM was able to capture Reynolds stresses and their corresponding statistics similar to the EL and EE-AG models at the center of the channel, there was significant deviation in the RSM predictions close to the wall.

At greater mass loadings the RSM was able to capture the same behaviors of the particle volume fraction. The small particles featured areas of high concentration that were long and stringlike down the length of the channel, which were also observed in the EE-AG model. At lower mass loadings using small particles, the RSM particle volume fraction featured a preferential concentration at the center of channel that was not observed in the EE-AG or EL results. The large-particle cases did not display any transient clustering down the length of the channel as was observed in the most concentrated EE-AG case. The model introduced in this work was able to emulate many of the changes in turbulence observed in the EL and EE-AG models as the mass loading was also changed. The RSM was able to capture the increase in particle- and fluid-phase anisotropy in the Reynolds stresses at higher mass loadings found in the other models. Additionally, the fluid-phase turbulence declined in the center of the channel as particles were initially added for both the large- and small-particle cases. While the large-particle cases were able to demonstrate a recovery in the fluid-phase turbulence from CIT as even more particles were added, the same was not true for the

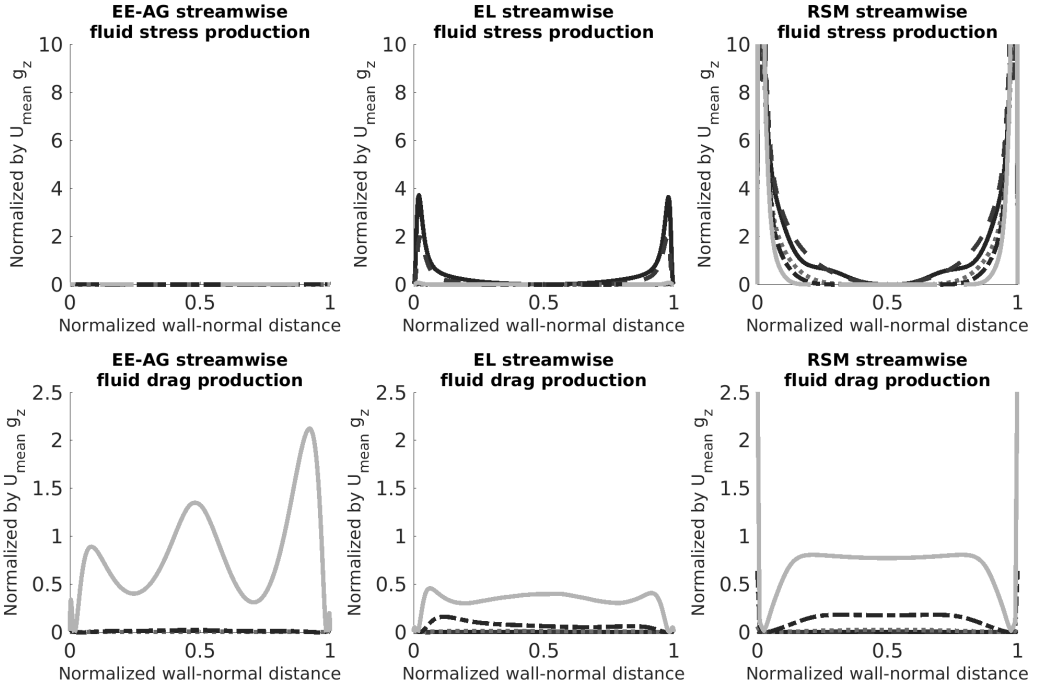

FIG. 15. Fluid-phase streamwise Reynolds-stress turbulent-production and drag-production terms with large particles. ML = 0.2 cases are denoted as (▬▬), ML = 1 cases are denoted as (▬ ▬), ML = 2 cases are denoted as (▪▪▪▪▪), ML = 4 cases are denoted as (▬ ▪ ▬), and ML=10 cases are denoted as (▬▬).

small-particle cases. The reason behind this was that the drag coefficient extracted from the EL underpredicted the amount of turbulent drag production for the small-particle cases.

Overall, the RSM introduced in this work presents a basis from which further study on how turbulent statistics extracted from more computationally expensive models can be applied to further improve its results. The limited parameter modifications implemented in this work demonstrate this potential. Additional exploration of the behavior of the many parameters and terms involved with the RSM for both phases and how they change based on flow conditions such as local particle concentration or proximity to a wall is needed to improve the incongruities with the other models observed in the current results. The development of a wall model applicable to low-Reynolds-number behavior and a variety of mass loadings is essential for getting accurate results for wall-bounded flow in systems such as this. Given the number of parameters and the degree of complexity of balancing their interconnected impacts on the overall model, machine-learning techniques present an extremely enticing path to go down. Additionally, isolating various turbulence model parameters and terms in simpler domains or systems such as homogeneous shear flow offers another way to more clearly understand their behavior.

APPENDIX A: REYNOLDS-STRESS MODEL TABLES OF EQUATIONS

Tables V, VI, VII, and VIII contain the complete system of equations applied in the RSM simulations introduced in this work.

TABLE V. Reynolds-stress model equations part I.

Particle-phase continuity

$$\frac{\partial \langle \alpha_p \rangle}{\partial t} + \frac{\partial \langle \alpha_p \rangle \langle u_{p,i} \rangle_p}{\partial x_i} = 0$$

Fluid-phase momentum transport

$$\frac{\partial \rho_f \langle \alpha_f \rangle \langle u_{i,f} \rangle_f}{\partial t} + \frac{\partial}{\partial x_j} \rho_f \langle \alpha_f \rangle (\langle u_{i,f} \rangle_f \langle u_{f,j} \rangle_f + \langle u'''_{f,j} u'''_{f,i} \rangle_f) = S_{f,\text{momentum},i}$$

$$S_{f,\text{momentum},i} = S_{f,\text{viscous},i} + S_{f,\text{pressure},i} + S_{f,\text{gravity},i} + S_{f,\text{drag},i}$$

$$S_{f,\text{viscous},i} = \frac{\partial}{\partial x_j} \rho_f \langle \alpha_f \rangle \nu_f \left(\frac{\partial \langle u_{f,i} \rangle_f}{\partial x_j} + \frac{\partial \langle u_{f,j} \rangle_f}{\partial x_i} - \frac{2}{3} \frac{\partial \langle u_{f,k} \rangle_f}{\partial x_k} \delta_{ij} \right)$$

$$S_{f,\text{pressure},i} = -\frac{\partial \langle p_f \rangle}{\partial x_i}$$

$$S_{f,\text{gravity},i} = \rho_f \langle \alpha_f \rangle g_i$$

$$S_{f,\text{drag},i} = \frac{\rho_p \langle \alpha_p \rangle}{\tau_p} (1 - c_g)(\langle u_{p,i} \rangle_p - \langle u_{f,i} \rangle_f)$$

$$\tau_p = \frac{d_p^2 \rho_p}{18 \nu_f \rho_f}$$

Particle-phase momentum transport

$$\frac{\partial \rho_p \langle \alpha_p \rangle \langle u_{i,p} \rangle_p}{\partial t} + \frac{\partial}{\partial x_j} \rho_p \langle \alpha_p \rangle (\langle u_{i,p} \rangle_p \langle u_{p,j} \rangle_p + \langle u''_{p,j} u''_{p,i} \rangle_p) = S_{p,\text{momentum},i}$$

$$S_{p,\text{momentum},i} = S_{p,\text{viscous},i} + S_{p,\text{pressure},i} + S_{p,\text{collision},i} + S_{p,\text{gravity},i} + S_{p,\text{drag},i}$$

$$S_{p,\text{viscous},i} = \frac{\partial}{\partial x_j} \rho_p \langle \alpha_p \rangle \nu_p \left(\frac{\partial \langle u_{p,i} \rangle_p}{\partial x_j} + \frac{\partial \langle u_{p,j} \rangle_p}{\partial x_i} - \frac{2}{3} \frac{\partial \langle u_{p,k} \rangle_p}{\partial x_k} \delta_{ij} \right)$$

$$\nu_p = \frac{\sqrt{\pi}}{6(3-e_c)} d_p \sqrt{\langle \Theta_p \rangle_p} \left(1 + \frac{2}{5}(1+e_c)(3e_c - 1)\langle \alpha_p \rangle g_0\right) + \frac{4(1+e_c)}{5\sqrt{\pi}} \langle \alpha_p \rangle g_0 d_p \sqrt{\langle \Theta_p \rangle_p}$$

$$g_0 = \frac{1}{1 - \left(\frac{\langle \alpha_p \rangle}{\alpha_{p,\max}}\right)^{1/3}}$$

$$S_{p,\text{pressure},i} = -\frac{\partial \rho_p \langle \alpha_p \rangle \langle \mathcal{P}_{p,ij} \rangle_p}{\partial x_j}$$

$$S_{p,\text{collision},i} = -\frac{\partial \rho_p \langle \alpha_p \rangle \langle \mathcal{G}_{p,ij} \rangle_p}{\partial x_j}$$

$$\langle \mathcal{G}_{p,ij} \rangle_p = \frac{2}{5}(1+e_c)\langle \alpha_p \rangle g_0 (\langle \mathcal{P}_{p,kk} \rangle_p \delta_{ij} + 2\langle \mathcal{P}_{p,ij} \rangle_p)$$

$$S_{p,\text{gravity},i} = \rho_p \langle \alpha_p \rangle g_i$$

$$S_{p,\text{drag},i} = \frac{\rho_p \langle \alpha_p \rangle}{\tau_p} (1 - c_g)(\langle u_{f,i} \rangle_f - \langle u_{p,i} \rangle_p)$$

TABLE VI. Reynolds-stress model equations part II.

Fluid-phase Reynolds-stress transport

$$\frac{\partial \rho_f \langle \alpha_f \rangle \langle u'''_{f,i} u'''_{f,j} \rangle_f}{\partial t} + \frac{\partial \rho_f \langle \alpha_f \rangle \langle u'''_{f,i} u'''_{f,j} \rangle_f \langle u_{f,k} \rangle_f}{\partial x_k} = S_{f,\text{stress},ij}$$

$$S_{f,\text{stress},ij} = S_{f,\text{flux},ij} + S_{f,\text{production},ij} + S_{f,\text{pressure-strain},ij} + S_{f,\text{dragstress},ij} + S_{f,\text{dissipation},ij} + S_{f,\text{interphase},ij}$$

$$S_{f,\text{flux},ij} = \frac{\partial}{\partial x_k} \rho_f \langle \alpha_f \rangle_f (\nu_f + \frac{\nu_{f,T}}{\eta_k}) \frac{\partial \langle u'''_{f,i} u'''_{f,j} \rangle_f}{\partial x_k}$$

$$\nu_{f,T} = c_{f,\mu} \frac{k_f^2}{\varepsilon_f}$$

$$S_{f,\text{production},ij} = \rho_f \langle \alpha_f \rangle P_{f,ij}$$

$$P_{f,ij} = -\langle u'''_{f,i} u'''_{f,k} \rangle_f \frac{\partial \langle u_{f,j} \rangle_f}{\partial x_k} - \langle u'''_{f,j} u'''_{f,k} \rangle_f \frac{\partial \langle u_{f,i} \rangle_f}{\partial x_k}$$

$$S_{f,\text{pressure-strain},ij} = -\frac{\rho_f \langle \alpha_f \rangle \varepsilon_f}{k_f} c_{1,f} (\langle u'''_{f,i} u'''_{f,j} \rangle_f - \tfrac{2}{3} k_f \delta_{ij}) - \rho_f \langle \alpha_f \rangle c_{2,f} (P_{f,ij} - \tfrac{1}{3} P_{f,kk} \delta_{ij}) - \rho_f \langle \alpha_f \rangle c_D (P_{g,ij} - \tfrac{1}{3} P_{g,kk} \delta_{ij})$$

$$P_{g,ij} = \frac{2}{\tau_p} c_g (\langle u_{f,k} \rangle_f - \langle u_{p,k} \rangle_p)^2 \delta_{ik} \delta_{jk}$$

$$S_{f,\text{dragstress},ij} = \rho_p \langle \alpha_p \rangle P_{g,ij}$$

$$S_{f,\text{dissipation},ij} = -\rho_f \langle \alpha_f \rangle \epsilon_{f,ij}$$

$$\epsilon_{f,ij} = (c_f \frac{\langle u'''_{f,i} u'''_{f,j} \rangle_f}{k_f} + \tfrac{2}{3}(1 - c_f) \delta_{ij}) \varepsilon_f$$

$$S_{f,\text{interphase},ij} = \frac{2 \rho_p \langle \alpha_p \rangle}{\tau_p} (\beta_{fp} \gamma_{sgn,ij} |\langle u'''_{f,i} u'''_{f,j} \rangle_f \langle u''_{p,i} u''_{p,j} \rangle_p|^{1/2} - \beta_f \langle u'''_{f,i} u'''_{f,j} \rangle_f)$$

$$\gamma_{sgn,ij} = \begin{cases} \text{sgn}(\langle u'''_{f,i} u'''_{f,j} \rangle_f) & \text{if sgn}(\langle u'''_{f,i} u'''_{f,j} \rangle_f) = \text{sgn}(\langle u''_{p,i} u''_{p,j} \rangle_p), \\ 0 & \text{otherwise.} \end{cases}$$

Fluid-phase turbulent dissipation transport

$$\frac{\partial \rho_f \langle \alpha_f \rangle \varepsilon_f}{\partial t} + \frac{\partial \rho_f \langle \alpha_f \rangle \varepsilon_f \langle u_{f,i} \rangle_f}{\partial x_i} = S_{f,\text{dissipation}}$$

$$S_{f,\text{dissipation}} = S_{\varepsilon_f,\text{flux}} + S_{\varepsilon_f,\text{generation}} + S_{\varepsilon_f,\text{destruction}} + S_{\varepsilon_f,\text{interphase}} + S_{\varepsilon_f,\text{drag}}$$

$$S_{\varepsilon_f,\text{flux}} = \frac{\partial}{\partial x_i} \rho_f \langle \alpha_f \rangle (\nu_f + \frac{\nu_{f,T}}{\eta_\varepsilon}) \frac{\partial \varepsilon_f}{\partial x_i}$$

$$S_{\varepsilon_f,\text{generation}} = \frac{\rho_f \langle \alpha_f \rangle \varepsilon_f}{2 k_f} c_{\varepsilon 1} P_{f,kk}$$

$$S_{\varepsilon_f,\text{destruction}} = -\frac{\rho_f \langle \alpha_f \rangle \varepsilon_f}{k_f} c_{\varepsilon 2} \varepsilon_f$$

$$S_{\varepsilon_f,\text{interphase}} = \frac{2 \rho_p \langle \alpha_p \rangle}{\tau_p} c_{\varepsilon 3} (\beta_{fp} \sqrt{\varepsilon_f \varepsilon_p} - \beta_f \varepsilon_f)$$

$$S_{\varepsilon_f,\text{drag}} = \frac{\rho_p \langle \alpha_p \rangle \varepsilon_p}{k_p} c_{\varepsilon 4} P_{g,kk}$$

TABLE VII. Reynolds-stress model equations part III.

Particle-phase Reynolds-stress transport

$$\frac{\partial \rho_p \langle\alpha_p\rangle \langle u''_{p,i} u''_{p,j}\rangle_p}{\partial t} + \frac{\partial \rho_p \langle\alpha_p\rangle \langle u''_{p,i} u''_{p,j}\rangle_p \langle u_{p,k}\rangle_p}{\partial x_k} = S_{p,\text{stress},ij}$$

$$S_{p,\text{stress},ji} = S_{p,\text{flux},ij} + S_{p,\text{production},ij} + S_{p,\text{pressure-strain},ij} + S_{p,\text{dissipation},ij} + S_{p,\text{interphase},ij}$$

$$S_{p,\text{flux},ij} = \frac{\partial}{\partial x_k} \rho_p \langle\alpha_p\rangle_p ((\nu_p + \frac{\nu_{p,T}}{\eta_k}) \frac{\partial \langle u''_{p,i} u''_{p,j}\rangle_p}{\partial x_k} + \frac{\nu_{p,T}}{\eta_k} \frac{\partial \langle\Theta_p\rangle_p}{\partial x_k} \delta_{ij})$$

$$\nu_{p,T} = c_{p,\mu} \frac{k_p^2}{\varepsilon_p}$$

$$S_{p,\text{production},ij} = \rho_p \langle\alpha_p\rangle P_{p,ij}$$

$$P_{p,ij} = -\langle u''_{p,i} u''_{p,k}\rangle_p \frac{\partial \langle u_{p,j}\rangle_p}{\partial x_k} - \langle u''_{p,j} u''_{p,k}\rangle_p \frac{\partial \langle u_{p,i}\rangle_p}{\partial x_k}$$

$$S_{p,\text{pressure-strain},ij} = \frac{\rho_p \langle\alpha_p\rangle \varepsilon_p}{k_p} c_{1,p} (\langle u''_{p,i} u''_{p,j}\rangle_p - \tfrac{2}{3} k_p \delta_{ij}) - \rho_p \langle\alpha_p\rangle c_{2,p} (P_{p,ij} - \tfrac{1}{3} P_{p,kk} \delta_{ij})$$

$$S_{p,\text{dissipation},ij} = -\rho_p \langle\alpha_p\rangle \epsilon_{p,ij}$$

$$\epsilon_{p,ij} = (c_p \frac{\langle u''_{p,i} u''_{p,j}\rangle_p}{k_p} + \tfrac{2}{3}(1 - c_p)\delta_{ij})\varepsilon_p$$

$$S_{p,\text{interphase},ij} = \frac{2\rho_p \langle\alpha_p\rangle}{\tau_p} (\beta_{fp} \gamma_{sgn,ij} |\langle u'''_{f,i} u'''_{f,j}\rangle_f \langle u''_{p,i} u''_{p,j}\rangle_p|^{1/2} - \langle u'''_{p,i} u'''_{p,j}\rangle_p)$$

Particle-phase turbulent dissipation transport

$$S_{p,\text{dissipation}} = S_{\varepsilon_p,\text{flux}} + S_{\varepsilon_p,\text{generation}} + S_{\varepsilon_p,\text{destruction}} + S_{\varepsilon_p,\text{interphase}}$$

$$S_{\varepsilon_p,\text{flux}} = \frac{\partial}{\partial x_i} \rho_p \langle\alpha_p\rangle (\nu_p + \frac{\nu_{p,T}}{\eta_\varepsilon}) \frac{\partial \varepsilon_p}{\partial x_i}$$

$$S_{\varepsilon_p,\text{generation}} = \frac{\rho_p \langle\alpha_p\rangle \varepsilon_p}{2k_p} c_{\varepsilon 1} P_{p,kk}$$

$$S_{\varepsilon_p,\text{destruction}} = -\frac{\rho_p \langle\alpha_p\rangle \varepsilon_p}{k_p} c_{\varepsilon 2} \varepsilon_p$$

$$S_{\varepsilon_p,\text{interphase}} = \frac{2\rho_p \langle\alpha_p\rangle}{\tau_p} c_{\varepsilon 3} (\beta_{fp} \sqrt{\varepsilon_f \varepsilon_p} - \varepsilon_p)$$

TABLE VIII. Reynolds-stress model equations part IV.

Particle-phase pressure transport

$$\frac{\partial \rho_p \langle\alpha_p\rangle \langle \mathcal{P}_{p,ij}\rangle_p}{\partial t} + \frac{\partial \rho_p \langle\alpha_p\rangle \langle \mathcal{P}_{p,ij}\rangle_p \langle u_{p,k}\rangle_p}{\partial x_k} = S_{\boldsymbol{\mathcal{P}},ij}$$

$$S_{\boldsymbol{\mathcal{P}},ij} = S_{\boldsymbol{\mathcal{P}},\text{flux},ij} + S_{\boldsymbol{\mathcal{P}},\text{dissipation},ij} + S_{\boldsymbol{\mathcal{P}},\text{generation},ij} + S_{\boldsymbol{\mathcal{P}},\text{collision},ij} + S_{\boldsymbol{\mathcal{P}},\text{interphase},ij}$$

$$S_{\boldsymbol{\mathcal{P}},\text{flux},ij} = \frac{\partial}{\partial x_k} \rho_p \langle\alpha_p\rangle (\kappa_p + \frac{\nu_{p,T}}{\eta_\Theta}) \frac{\partial \langle \mathcal{P}_{p,ij}\rangle_p}{\partial x_k}$$

$$\kappa_p = \frac{\nu_p}{\text{Pr}_p}$$

$$\text{Pr}_p = \frac{16 - 11 e_c}{15 - 5 e_c}$$

$$S_{\boldsymbol{\mathcal{P}},\text{dissipation},ij} = \rho_p \langle\alpha_p\rangle \epsilon_{p,ij}$$

$$S_{\boldsymbol{\mathcal{P}},\text{generation},ij} = -\rho_p \langle\alpha_p\rangle ((\langle \mathcal{P}_{p,ik}\rangle_p + \langle \mathcal{G}_{p,ik}\rangle_p) \frac{\partial \langle u_{p,j}\rangle_p}{\partial x_k} + (\langle \mathcal{P}_{p,jk}\rangle_p + \langle \mathcal{G}_{p,jk}\rangle_p) \frac{\partial \langle u_{p,i}\rangle_p}{\partial x_k})$$

$$S_{\boldsymbol{\mathcal{P}},\text{collision},ij} = \frac{2\rho_p \langle\alpha_p\rangle}{\tau_c} (\Delta^*_{ij} - \langle \mathcal{P}_{p,ij}\rangle_p)$$

$$\Delta^*_{ij} = \frac{(1 + e_c)^2}{4} \langle\Theta_p\rangle_p \delta_{ij} + \frac{(1 - e_c)^2}{4} \langle \mathcal{P}_{p,ij}\rangle_p$$

$$\tau_c = \frac{d_p}{6\langle\alpha_p\rangle g_0 (\frac{\langle\Theta_p\rangle_p}{\pi})^{1/2}}$$

$$S_{\boldsymbol{\mathcal{P}},\text{interphase},ij} = -\frac{2\rho_p \langle\alpha_p\rangle}{\tau_p} \langle \mathcal{P}_{p,ij}\rangle_p$$

APPENDIX B: NOMENCLATURE

Tables IX, X, and XI contain the definitions and nominal values where applicable for the parameters and variables applied in this work.

TABLE IX. Nomenclature and nominal values of parameters part I.

C	11	Low-Reynolds-number wall parameter
C_{CFL}		Courant number from the Courant-Friedrichs-Lewy (CFL) condition
C_{Θ}		Wall granular energy redistribution coefficient
$c_{1,n}$		Phase pressure-strain Reynolds-stress redistribution coefficient
$c_{2,n}$		Phase pressure-strain production redistribution coefficient
c_c	2	Collision coefficient
c_D		Pressure-strain drag redistribution coefficient
c_g		Drift velocity coefficient
c_n	0.93	Phase dissipation tensor blending coefficient
$c_{n,\mu}$	0.23	Phase turbulent viscosity coefficient
$c_{\varepsilon 1}$	1.44	Turbulent eddy generation dissipation coefficient
$c_{\varepsilon 2}$	1.92	Turbulent eddy destruction dissipation coefficient
$c_{\varepsilon 3}$	0.736	Turbulent interphase dissipation coefficient
$c_{\varepsilon 4}$	1.92	Turbulent drag dissipation coefficient
d_p	45, 150 μm	Particle diameter
e_c	0.9	Particle restitution coefficient
e_w	1	Wall restitution coefficient
g_0		Radial distribution function
g_i		Gravitational acceleration
K_{drag}		Overall drag coefficient
k_n		Phase turbulent kinetic energy
k_{Θ}		Granular conductivity coefficient
Ma_p		Particle-phase Mach number

TABLE X. Nomenclature and nominal values of parameters part II.

$P_{g,ij}$		Drag production tensor
$P_{n,ij}$		Phase production tensor
$P_{n,\varepsilon\text{wall},ii}$		Near-wall modeled production tensor
Pr_p		Granular Prandtl number
p_f		Fluid-phase pressure
Re_f		Fluid Reynolds number
$\mathbf{S}$		Cell surface
S_n		Phase source or sink term
$u_{n,i}$		Phase velocity
$u'''_{f,i}$		Fluctuating component of fluid velocity
$u''_{p,i}$		Fluctuating component of particle velocity
$\langle u'''_{f,i} u'''_{f,j} \rangle$		Fluid-phase Reynolds-stress tensor
$\langle u''_{p,i} u''_{p,j} \rangle$		Particle-phase Reynolds-stress tensor
V		Cell volume
y_n^+		Phase boundary layer coordinate
$\mathbb{A}$		Diagonal coefficients
$\mathcal{D}_w$		Granular energy production from wall slip
$\mathcal{D}_\Theta$		Granular energy production from wall collisions
$\mathcal{E}$	9.0	Wall roughness coefficient
$\mathcal{G}_{p,ij}$		Collisional pressure tensor
$\mathbb{H}$		Off-diagonal contributions to the fluid-phase equation
$\mathcal{P}_{p,ij}$		Particle-phase pressure tensor
$\mathcal{V}_w$		Wall collision velocity

TABLE XI. Nomenclature and nominal values of parameters part III.

α_n		Phase volume fraction
$\alpha_{p,\max}$	0.63	Maximum packing fraction
β_f	1.03	Interphase drift coefficient
β_{fp}	0.876	Interphase correlation coefficient
$\beta_{w,ij}$		Pure-fluid wall redistribution tensor
γ_f		Inverse sum of the diagonal coefficients and overall drag coefficient
$\gamma_{n,ij}$		Phase wall boundary anisotropy coefficient
$\gamma_{sgn,ig}$		Asymmetric sign control coefficient
η_ε	1	Turbulent viscosity dissipation coefficient
η_k	1	Turbulent viscosity coefficient
$\eta_{n,\mathrm{iso}}$		Phase anisotropy parameter
η_Θ	1	Turbulent Prandtl number
Δ^*		Collisional energy source term
Δ_{wall}		Wall-normal mesh length of near-wall cells
ε_n		Phase turbulent dissipation
$\epsilon_{n,ij}$		Phase turbulent dissipation tensor
κ	0.41	von Kármán constant
κ_p		Granular conductivity coefficient
ϕ		Phase mass loading ratio
ϕ_s	0	Specularity coefficient
ϕ_n		Phase surface velocity flux
ρ_n		Phase density
τ_c		Particle collision timescale
τ_p		Stokes drag model constant
Θ_p		Granular temperature
ν_n		Phase viscosity
$\nu_{n,T}$		Phase turbulent viscosity

[1] R. O. Fox, Large-eddy-simulation tools for multiphase flows, Annu. Rev. Fluid Mech. **44**, 47 (2012).

[2] M. A. van der Hoef, M. Ye, M. van Sint Annaland, A. T. Andrews, S. Sundaresan, and J. A. M. Kuipers, *Multiscale Modeling of Gas-Fluidized Beds*, Advances in Chemical Engineering Vol. 1 (Elsevier, New York, 2006), pp. 65–149.

[3] J. G. M. Kuerten, Point-particle DNS and LES of particle-laden turbulent flow—A state-of-the-art review, Flow, Turb. Combust. **97**, 689 (2016).

[4] Z. Feng and S. G. Musong, Direct numerical simulation of heat and mass transfer of spheres in a fluidized bed, Powder Technol. **262**, 62 (2014).

[5] T. Pan, D. D. Joseph, R. Bai, R. Glowinski, and V. Sarin, Fluidization of 1204 spheres: Simulation and experiment, J. Fluid Mech. **451**, 169 (2002).

[6] S. Tenneti and S. Subramaniam, Particle-resolved direct numerical simulation for gas–solid flow model development, Annu. Rev. Fluid Mech. **46**, 199 (2014).

[7] Y. Li, J. B. McLaughlin, K. Kontomaris, and L. Portela, Numerical simulation of particle-laden turbulent channel flow, Phys. Fluids **13**, 2957 (2001).

[8] J. Lee and C. Lee, Modification of particle-laden near-wall turbulence: Effect of Stokes number, Phys. Fluids **27**, 023303 (2015).

[9] C. D. Dritselis and N. S. Vlachos, Numerical study of educed coherent structures in the near-wall region of a particle-laden channel flow, Phys. Fluids **20**, 055103 (2008).

[10] P. Costa, L. Brandt, and F. Picano, Interface-resolved simulations of small inertial particles in turbulent channel flow, J. Fluid. Mech. **883**, A54 (2020).

[11] G. Wang, K. O. Fong, F. Coletti, J. Capecelatro, and D. H. Richter, Inertial particle velocity and distribution in vertical turbulent channel flow: A numerical and experimental comparison, Int. J. Multiphase Flow **120**, 103105 (2019).
[12] N. A. Patankar and D. D. Joseph, Modeling and numerical simulation of particulate flows by the Eulerian–Lagrangian approach, Int. J. Multiphase Flow **27**, 1659 (2001).
[13] J. Capecelatro and O. Desjardins, An Euler–Lagrange strategy for simulating particle-laden flows, J. Comput. Phys. **238**, 1 (2013).
[14] B. Vreman, B. J. Geurts, N. G. Deen, J. A. M. Kuipers, and J. G. M. Kuerten, Two- and four-way coupled Euler–Lagrangian large-eddy simulation of turbulent particle-laden channel flow, Flow, Turb. Combust. **82**, 47 (2009).
[15] T. B. Anderson and R. Jackson, Fluid mechanical description of fluidized beds: Equations of motion, Ind. Eng. Chem. Fundam. **6**, 527 (1967).
[16] D. A. Drew, Mathematical modeling of two-phase flow, Annu. Rev. Fluid Mech. **15**, 261 (1983).
[17] T. Kajishima, S. Takiguchi, H. Hamasaki, and Y. Miyake, Turbulence structure of particle-laden flow in a vertical plane channel due to vortex shedding, JSME Int. J., Ser. B **44**, 526 (2001).
[18] D. Gidaspow, *Multiphase Flow and Fluidization: Continuum and Kinetic Theory Descriptions*, (Academic Press, New York, 2012).
[19] J. Capecelatro, O. Desjardins, and R. O. Fox, Strongly coupled fluid–particle flows in vertical channels, II. Turbulence modeling, Phys. Fluids **28**, 033307 (2016).
[20] R. O. Fox, On multiphase turbulence models for collisional fluid–particle flows, J. Fluid Mech. **742**, 368 (2014).
[21] T. Ma, D. Lucas, S. Jakirlic, and J. Fröhlich, Progress in the second-moment closure for bubbly flow based on direct numerical simulation data, J. Fluid Mech. **883**, A9 (2019).
[22] A. Rao, J. S. Curtis, B. C. Hancock, and C. Wassgren, Numerical simulation of dilute turbulent gas–particle flow with turbulence modulation, AIChE J. **58**, 1381 (2012).
[23] C. D. Dritselis, Direct numerical simulation of particle-laden turbulent channel flows with two- and four-way coupling effects: Budgets of Reynolds stress and streamwise enstrophy, Fluid Dyn. Res. **48**, (2016).
[24] J. Capecelatro, O. Desjardins, and R. O. Fox, On the transition between turbulence regimes in particle-laden channel flows, J. Fluid Mech. **845**, 499 (2018).
[25] M. H. Kasbaoui, D. L. Koch, and O. Desjardins, Clustering in Euler–Euler and Euler–Lagrange simulations of unbounded homogeneous particle-laden shear, J. Fluid Mech. **859**, 174 (2019).
[26] W. D. Fullmer and C. M. Hrenya, The clustering instability in rapid granular and gas–solid flows, Annu. Rev. Fluid Mech. **49**, 485 (2017).
[27] A. du Cluzeau, G. Bois, and A. Toutant, Analysis and modeling of Reynolds stresses in turbulent bubbly up-flows from direct numerical simulations, J. Fluid Mech. **866**, 132 (2019).
[28] P. Février, O. Simonin, and K. D. Squires, Partitioning of particle velocities in gas–solid turbulent flows into a continuous field and a spatially uncorrelated random distribution: Theoretical formalism and numerical study, J. Fluid Mech. **533**, 1 (2005).
[29] J. Capecelatro, O. Desjardins, and R. O. Fox, Strongly coupled fluid–particle flows in vertical channels, I. Reynolds-averaged two-phase turbulence statistics, Phys. Fluids **28**, 033306 (2016).
[30] B. Kong, R. O. Fox, H. Feng, J. Capecelatro, R. Patel, O. Desjardins, and R. O. Fox, Euler–Euler anisotropic Gaussian mesoscale simulation of homogeneous cluster-induced gas–particle turbulence, AIChE J. **63**, 2630 (2017).
[31] S. B. Pope, *Turbulent Flows* (Cambridge University Press, Cambridge, England, 2000).
[32] M. C. Baker, B. Kong, J. Capecelatro, O. Desjardins, and R. O. Fox, Direct comparison of Eulerian–Eulerian and Eulerian–Lagrangian simulations for particle-laden vertical channel flow, AIChE J. **66**, e16230 (2020).
[33] D. Wilcox, *Turbulence Modeling for CFD* (DCW Industries, Inc., New York, 1994).
[34] J. Capecelatro, O. Desjardins, and R. O. Fox, Numerical study of collisional particle dynamics in cluster-induced turbulence, J. Fluid Mech. **747**, R21 (2014).
[35] J. Rotta, Statistische theorie nichthomogener turbulenz, Z. Phys. **129**, 547 (1951).

[36] J. Capecelatro, O. Desjardins, and R. O. Fox, On fluid–particle dynamics in fully developed cluster-induced turbulence, J. Fluid Mech. **780**, 578 (2015).

[37] A. Passalacqua, J. E. Galvin, P. Vedula, C. M. Hrenya, and R. O. Fox, A quadrature-based kinetic model for dilute non-isothermal granular flows, Commun. Comput. Phys. **10**, 216 (2011).

[38] J. Kim, P. Moin, and R. Moser, Turbulence statistics in fully developed channel flow at low Reynolds number, J. Fluid Mech. **177**, 133 (1987).

[39] ANSYS Fluent Theory Guide, *SAS IP, Inc.*, 15.0 edition (Canonsburg PA, 2013).

[40] S. Liu, Implementation of a complete wall function for the standard k–ϵ turbulence model in OpenFOAM 4.0, Technical report, University of Stavanger, 2017.

[41] M. M. Gibson and B. E. Launder, Ground effects on pressure fluctuations in the atmospheric boundary layer, J. Fluid Mech. **86**, 491 (1978).

[42] J. S. Curtis and B. Van Wachem, Modeling particle-laden flows: A research outlook, AIChE J. **50**, 2638 (2004).